Examination of the traditional Raman lidar technique. I. Evaluating the temperature-dependent lidar equations

David N. Whiteman

The essential information required for the analysis of Raman lidar water vapor and aerosol data acquired by use of a single laser wavelength is compiled here and in a companion paper [Appl. Opt. **42,** 2593 (2003)]. Various details concerning the evaluation of the lidar equations when Raman scattering is measured are covered. These details include the influence of the temperature dependence of both pure rotational and vibrational–rotational Raman scattering on the lidar profile. The full temperature dependence of the Rayleigh–Mie and Raman lidar equations are evaluated by use of a new form of the lidar equation where all the temperature dependence is carried in a single term. The results indicate that, for the range of temperatures encountered in the troposphere, the magnitude of the temperature-dependent effect can reach 10% or more for narrowband Raman water-vapor measurements. Also, the calculation of atmospheric transmission, including the effects of depolarization, is examined carefully. Various formulations of Rayleigh cross-section determination commonly used in the lidar field are compared and reveal differences of as much as 5% among the formulations. The influence of multiple scattering on the measurement of aerosol extinction with the Raman lidar technique is considered, as are several photon pulse pileup-correction techniques.

OCIS codes: 010.3640, 010.3920.

1. Introduction

The Raman lidar is well established today as a leading research tool in the study of numerous areas of importance in the atmospheric sciences. The Raman lidar has been used to study the passage of frontal systems,[1] stratospheric aerosols that result from volcanic eruptions,[2] atmospheric temperature variations in cirrus clouds,[3] long-term variation of water vapor and aerosols at a mid-continental site,[4] cloud liquid water,[5] cirrus cloud optical[6] and physical[7] properties, the influence of thin cirrus clouds on satellite retrievals of water vapor,[8] hygroscopic growth of aerosols,[9] detection of cloud base height,[10] multiwavelength Raman lidar measurements of aerosols to permit remote characterization of aerosols,[11,12] and other topics. Recently, numerical simulation was used to demonstrate that airborne Raman water-vapor lidar offers a dramatic increase in temporal and spatial resolution compared with existing differential absorption lidars under nighttime conditions.[13] Of all these uses of Raman lidar, perhaps the most common has been for the measurement of water vapor and aerosols by use of either a UV or a visible radiation source. Yet, despite the availability of several good publications that describe these measurements of water vapor and aerosols,[1,4,9,14–20] the essential material needed for analyzing these Raman lidar data has not previously been compiled in a single publication. With several new Raman lidars being developed as a part of the European Aerosol Lidar Network[21,22] (EARLINET) and other activities, it seems an appropriate time to create such a reference. Furthermore, and perhaps more importantly, recent advances in the numerical simulation of the Raman water-vapor spectrum now permit the full effects of the temperature dependence of the individual spectral lines to be easily evaluated, as has been possible for the rotational Raman scattering from diatomic molecules[23–25] since the early days of lidar[26] and before.[27]

This first paper in a two-paper sequence addresses the details of evaluating the lidar equation, including the temperature sensitivity of Raman scattering. The companion paper[28] (referred to as part 2) then addresses the formation of ratios of lidar signals for the study of water vapor and aerosols. The general organization of this paper is as follows: First, as reference material, the traditional lidar equations

The author (david.n.whiteman@nasa.gov) is with NASA Goddard Space Flight Center, Greenbelt, Maryland 20771.

Received 28 January 2002; revised manuscript received 20 December 2002.

0003-6935/03/152571-22$15.00/0

are presented. Simulations of the temperature sensitivity of the Raman water-vapor spectrum are then presented, which offer motivation for development of a new form of temperature-dependent lidar equations in which the temperature dependence is confined to a single term. A detailed description of the calculation of atmospheric transmission including extinction that is due both to molecules and to aerosols in which the effects of temperature sensitivity are propagated through the aerosol extinction equations is then presented. Other effects that must be accounted for in the evaluation of the lidar equation are multiple scattering and photon pulse pileup. These are considered in appendixes.

2. Traditional Single-Scattering Rayleigh–Mie and Raman Lidar Equations

Equations are presented for Rayleigh–Mie and Raman lidars. To avoid confusion, a few definitions are given. The term "Rayleigh scattering" is used to signify the combination of Cabannes and rotational Raman scattering.[29,30] This definition recognizes the fact[29,30] that what Lord Rayleigh[31,32] actually detected was a combination of elastic and rotational Raman scattering. The term "Mie scattering" is used to refer to scattering by particles of any shape, even though the Mie theory[33] pertains only to spherical particles. The term "Rayleigh–Mie" lidar is then used here to refer to systems that measure elastically scattered light from both molecules and particles of any shape as well as inelastically scattered pure rotational Raman scattering. Finally, although changes in transmission versus wavelength are due mostly to the characteristics of the interference filter or monochromator used in a particular lidar channel, other optics in the system can also display wavelength-dependent transmission efficiency. Therefore the term "passband" is used to describe the transmission function of a particular lidar optical channel.

Now the background-subtracted power received by a detector as a function of range in a Rayleigh–Mie lidar system, assuming no multiple scattering and that the received signal is at a single discrete wavelength, can be expressed as

$$P(\lambda_L, r) = \frac{O(r) P_0(\lambda_L) A \xi(\lambda_L) \{N_R(r)[d\sigma_R(\lambda_L, \pi)/d\Omega] + \beta_\pi^{aer}(\lambda_L, r)\}}{r^2} \exp\left[-2 \int_0^r \alpha(\lambda_L, r')dr'\right], \quad (1)$$

where $P(\lambda_L, r)$ is the backscattered power (after any background contribution that is due, for example, to skylight or detector noise is subtracted) received at laser wavelength λ_L as a function of range r. $O_R(r)$ is the Rayleigh–Mie channel overlap function, and $P_0(\lambda_L)$ is the output power of the laser at laser wavelength λ_L. $N_R(r)$ is the number density of air molecules (Rayleigh scatterers), and $d\sigma_R(\lambda_L, \pi)/d\Omega$ is the Rayleigh backscatter cross section at the laser wavelength. $\beta_\pi^{aer}(\lambda_L, r)$ is the backscatter coefficient at the laser wavelength and at range r that is due to Mie scattering. $\xi(\lambda_L)$ is the total lidar receiver optical efficiency at the laser wavelength and includes factors such as the reflectivity of the telescope, the transmission of conditioning optics, the transmission of any filters, and the quantum efficiency of the detector. A is the receiver telescope area. The exponential factor gives the two-way atmospheric transmission, where $\alpha(\lambda_L, r)$ is the total extinction coefficient at the laser wavelength that is due to scattering and absorption by molecules, particles, and any other atmospheric constituents such as water droplets or ice crystals as a function of range along the path of the laser beam.

The corresponding single-scattering Raman lidar equation for a vibrationally scattered Raman species X, in its traditional form, is given by

$$P(\lambda_X, r) = \frac{O_X(r) P_0(\lambda_L) A \xi(\lambda_X) N_X(r)[d\sigma_X(\lambda_L, \pi)/d\Omega]}{r^2} \times \exp\left\{-\int_0^r [\alpha(\lambda_L, r') + \alpha(\lambda_X, r')]dr'\right\}, \quad (2)$$

where now it should be noted that the atmospheric transmission function includes a term at the laser wavelength, λ_L, for the transmission along the output path and another for the backscattered signal at the wavelength, λ_X, that has been shifted from the laser wavelength owing to inelastic Raman scattering by molecular species X. $N_X(r)$ is the number density of molecular species X that is being excited, and $d\sigma_X(\lambda_L, \pi)/d\Omega$ is the pertinent Raman backscatter cross section.

3. Temperature Dependence of the Lidar Equations

As stated, for Eqs. (1) and (2) it is assumed that the return signal can be considered to be at a discrete wavelength. In the case of the Raman signals excited in the visible or the near UV by lasers such as frequency-doubled (532.1-nm) or -tripled (354.7-nm) Nd:YAG, the desired signal actually covers an interval that can range from a few tenths of a nanometer (e.g., the OH-stretch region of water vapor) to a few nanometers (rotational–vibrational spectrum from diatomic molecules such as N_2 and O_2). In the case of the Rayleigh–Mie signal there is pure rotational Raman scattering from nitrogen, oxygen, and other molecules that is centered on the laser wavelength and that covers a band of a few nanometers as well.[34]

Therefore there is Raman scattering to be considered in both the Rayleigh–Mie and the Raman signals.

The individual line strengths in a Raman spectrum are temperature dependent. In general, this temperature dependence should be considered when one is formulating either the Rayleigh–Mie or the Raman lidar equations because, if the passband used to make the measurements transmits any Raman signals, the intensity of the backscattered signal per molecule may be temperature sensitive. This effect has been carefully considered by Sherlock *et al.*,[35] who developed temperature-dependent Raman lidar equations for calculations of the water-vapor mixing ratio. These earlier efforts accounted for the effects of temperature sensitivity in the absolute calibration of a water-vapor Raman lidar. However, their Raman scattering model did not include the anisotropic part of the water-vapor spectrum, which can now be included as a result of theoretical work that was performed recently.[36] The current ability to simulate the OH-stretch portion of the Raman water-vapor spectrum including the isotropic and anisotropic components eliminates one of the largest sources of error in the absolute calibration of a Raman water-vapor lidar that was pursued by Sherlock *et al.*[35] New forms of the lidar equations are derived here that will permit the temperature effect to be easily propagated through subsequent derivations.

To illustrate the effect of the temperature dependence of Raman scattering, let us consider the case of the Raman vibrational signals. The molecules are essentially all in their ground state at atmospheric temperatures as determined by the Maxwell–Boltzmann distribution. A vibrational Raman scattering event is therefore overwhelmingly likely to involve a transition from the ground state to the Stokes (higher-energy) part of the spectrum. Thus, at atmospheric temperatures, the integral across the entire Raman Stokes band will be temperature insensitive (the transition will appear somewhere in the spectrum). However, if only a portion of the band is transmitted, there will in general be a dependence of the transmitted intensity[37] on temperature, although there are some exceptions that are discussed below. For pure rotational Raman scattering, however, the rotational states differ little in energy from the ground state, so there is a significant probability that some of the rotational states will be excited at atmospheric temperatures. (With respect to the N_2 molecule, the $J = 0$ state for pure rotational Raman scattering is approximately 10^5 times more likely to be excited at $T = 290$ K than is the first vibrational transition). Thus the integral of neither the *O* nor the *S* branch of the rotational Raman spectrum is, by itself, temperature independent; however the sum of the two is.

If the lidar system's efficiency is constant over the wavelength interval that contains a complete Raman feature, either vibrational or pure rotational, then there is no temperature sensitivity to the received signals.[37] Also, there can be narrow portions of certain Raman spectra that are temperature independent. They exist, for example, at the isosbestic point of liquid water ($\sim$3425 cm^{-1}; Ref. 38) as well as in the spectral vicinity of $J = 7$, 8 for the pure rotational spectra of N_2 and O_2.[39] However, in general, if narrow passbands are used in the detection of Raman features, the total lidar system efficiency is likely to change as a function of temperature as the strengths of the individual lines in the Raman spectrum change,[35] imparting a temperature sensitivity to the measurement.

This temperature sensitivity can be useful for atmospheric measurements. The intensities of rotational and vibrational–rotational lines from N_2 and O_2 are well predicted by diatomic molecule line strength models.[23,27] These models have been used to facilitate atmospheric temperature measurements by use of Raman lidar.[3,26,40] These models are used here for evaluating the temperature sensitivity of the Raman pure rotational and vibrational–rotational N_2 and O_2 signals for various passband widths and center positions.

4. Raman Water-Vapor Simulations

Water is an asymmetric top molecule that possesses a much more complicated Raman spectrum than does either N_2 or O_2. The numerical simulation of the Raman spectrum from asymmetric top molecules such as water vapor was in the past available to a limited number of researchers.[41–44] However, a recent publication by Avila *et al.*[36] now makes it possible to easily simulate the Raman OH-stretch spectrum for water vapor over a range of temperatures. These results permit the anisotropic component of the Raman water-vapor spectrum to be included in the calculation, thus permitting the full temperature sensitivity of a Raman water-vapor lidar system to be evaluated for the first time to our knowledge.

This new modeling capability has been used to simulate spectra of the Raman OH-stretch region of water vapor at two temperatures, as shown in Fig. 1. These spectra have been simulated by use of 0.5-cm^{-1} resolution at 200 and 295 K. As temperature increases, the quantum number transitions that are farther from the band origin of 3657 cm^{-1} (i.e., higher J number) become increasingly more likely to be excited. This implies that, for a lidar system characterized by a narrow passband, simulated in the figure by a Gaussian transmission function of $\sim$18-cm^{-1} width (corresponding to $\sim$0.3 nm at $\sim$407.5 nm, the location of the water-vapor ν_1 transition when excited by the tripled Nd:YAG laser, 354.7 nm) and shown by a dashed–dotted curve, the integrated intensity of the Raman feature across the passband shown will be temperature sensitive. It should be mentioned that the atmospheric feature that is typically measured by a Raman water-vapor lidar is often referred to as the ν_1 band of water vapor. However, at atmospheric temperatures this portion of the spectrum also includes contributions from ν_3, which must be considered for accurate simulations of the spectra.[36] Contributions from ν_2 or its overtones are not significant below temperatures of $\sim$400 K.[45,46]

The Raman water-vapor differential backscatter

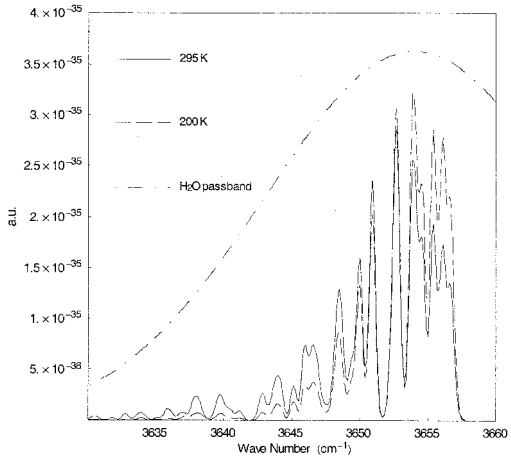

Fig. 1. Raman scattering spectrum for the OH-stretch region of water vapor simulated with a 0.5-cm^{-1} resolution and at two temperatures, 200 and 295 K. Also shown is a representation of an ~18-cm^{-1} (0.3 nm when it is excited at 354.7 nm) passband centered at 3654 cm^{-1} that can be used for detection of the water-vapor signal. The y axis is in arbitrary units.

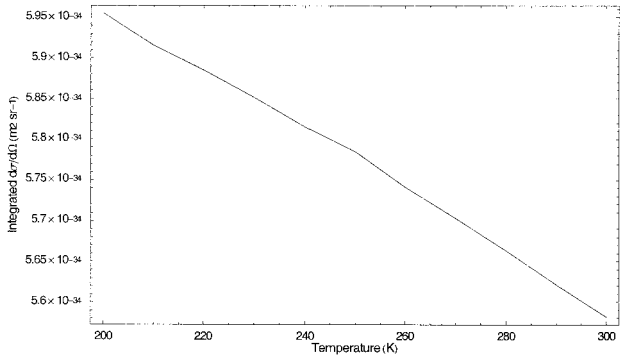

Fig. 2. Integral of the Raman differential backscatter cross section and transmission of the passband shown in Fig. 1. The transmitted intensity at 200 K is approximately 7% larger than at 300 K.

5. Temperature-Dependent Lidar Equations

A. Rayleigh–Mie Lidar Equation

The background-subtracted Rayleigh–Mie lidar equation, which is analogous to Eq. (1) but contains the temperature dependence of rotational Raman scattering explicitly, is

$$P(\lambda_L, \Delta\lambda_R, r) = \frac{O_R(r) P_0(\lambda_L) A \left\{ \int_{\Delta\lambda_R} [N_R(r) \mathrm{d}\sigma_R(\lambda', \pi, T[r])/\mathrm{d}\Omega] \xi(\lambda') \mathrm{d}\lambda' + \beta_\pi^{\mathrm{aer}}(\lambda_L, r) \xi(\lambda_L) \right\}}{r^2} \times \exp\left[-2 \int_0^r \alpha(\lambda_L, r') \mathrm{d}r' \right]. \quad (3)$$

cross section was determined for temperatures from 200 to 300 K for evaluation of the temperature sensitivity of the signal transmitted by the passband shown in Fig. 1. The integral of the passband centered at 3654 cm^{-1} shown in Fig. 1 and the Raman spectrum was performed at each of the temperatures. The results are plotted in Fig. 2. For these calculations, the area under the passband was normalized to unity. The results shown in Fig. 2 indicate that there is approximately a 7% change in transmitted intensity between 200 and 300 K. This implies that there would be an increase in the sensitivity of a narrowband Raman water-vapor lidar in the upper troposphere, where atmospheric temperatures are colder, compared with that at low altitudes.

These results suggest a reformulation of Eqs. (1) and (2) in a manner that makes this temperature dependence more explicit. One reformulation was published previously.[35] In Section 5 a new formulation is presented that permits all the temperature sensitivity of the equation to reside in a single term.

$P(\lambda_L, \Delta\lambda_R, r)$ is the background-subtracted, received power for passband $\Delta\lambda_R$, which contains the combined Rayleigh (Cabannes and rotational Raman) and Mie signals, as a function of range. This is the single-scattering lidar equation in a form that accounts for the possibility that the lidar system's optical efficiency, $\xi(\lambda')$, may change over the range of wavelengths $\Delta\lambda_R$, the wavelength range over which there is significant transmission of the Rayleigh–Mie signal by the lidar system. The subscript R is used to refer to the Rayleigh–Mie signal. It should be noted here that the laser bandwidth is implicitly assumed to be negligibly small. This is a good approximation when one is using commercial Nd:YAG lasers with bandwidths of ~1 cm^{-1} because narrowband interference filters that are used in Raman lidar studes are more than an order of magnitude wider than this. But XeF excimer lasers, for example, are known to possess an output spectrum ~2 nm wide covering the nominal laser emission wavelength of 351.1 nm.[37] In such a case an integral over the wavelengths covered by the laser output spectrum would be required in Eq. (3) for completeness.

The Rayleigh signal consists of a narrow elastically scattered signal at the laser wavelength (Cabannes scattering) along with inelastic (frequency-shifted) pure rotational lines that are due primarily to N_2 and O_2 on both sides of the Cabannes feature. For practical purposes, the rotational spectrum may be described by quantum numbers up to approximately 30,[47] which corresponds to a wavelength range of a few nanometers when the system is excited in the UV or the visible region. To measure this spectrum, the lidar system samples a range of wavelengths $\Delta\lambda_R$. It is possible that the lidar system's transmission efficiency will change over this wavelength range. The notation $d\sigma_R(\lambda', \pi, T)/d\Omega$, which includes the explicit wavelength and temperature dependences, is thus used for the differential backscatter cross section for the combined effects of Rayleigh and pure rotational Raman scattering. This formulation permits the influence of the changing intensity of the rotational Raman lines as a function of wavelength and temperature to be quantified. The temperature dependence of the rotational Raman lines can introduce a temperature sensitivity to the measured Rayleigh signal. Calculations of the rotational Raman line intensities of these diatomic molecules as a function of temperature,[23,27] coupled with knowledge of the lidar system's transmission characteristics, are needed for evaluating the temperature dependence of Eq. (3). Pure rotational scattering from other molecules such as carbon dioxide and water vapor[48] also exist, but at such small levels as to be insignificant for the present purposes.

Aerosols in the atmosphere are much heavier than molecules. The Doppler broadening of the Mie signal that is due to aerosols will therefore be much less than that for molecules. Therefore the Mie signal from aerosols has a narrower spectral width than the elastic scattering from molecules. Thus, for the passband widths considered here, the single-wavelength notation used in the traditional lidar equation for $\beta_\pi^{aer}(\lambda_L, r)$, the aerosol backscatter coefficient, and $\xi(\lambda_L)$, the total receiver system efficiency at the laser wavelength, are still appropriate in the temperature-dependent form of the equation.

B. Raman Lidar Equation

The temperature-dependent equation for the Raman signal species X is

$$P(\lambda_L, \Delta\lambda_X, r) = \frac{O_X(r) P_0(\lambda_L) N_X(r) A \int_{\Delta\lambda_X} [d\sigma_X(\lambda', \pi, T[r])/d\Omega]\xi(\lambda')d\lambda'}{r^2} \times \exp\left\{-\int_0^r [\alpha(\lambda_L, r') + \alpha(\lambda_X, r')]dr'\right\}, \quad (4)$$

where now $\Delta\lambda_X$ refers to the passband over which the Raman vibrational signal is detected. Notice here the lack of aerosol backscatter term $\beta_\pi^{aer}(\lambda_L, r)\xi(\lambda_L)$ because only inelastically scattered radiation owing to molecular interactions is present in this signal. A temperature-dependent function is now introduced that will permit Eqs. (3) and (4) to be expressed in a more straightforward manner. This temperature-dependent function simplifies previous formulations[35] and will permit the influence of temperature dependence to be easily propagated through the traditional Raman lidar formulas.[28]

C. Function $F_X(T)$

Consider the case of the vibrationally Raman-scattered signal from water vapor expressed by Eq. (4) with X replaced by H. The integral over $\Delta\lambda_H$ may be expressed as

$$\int_{\Delta\lambda_H} \frac{d\sigma_H(\lambda', \pi, T)}{d\Omega} \xi(\lambda')d\lambda' = F_H(T) \frac{d\sigma_H(\pi)}{d\Omega} \xi(\lambda_H), \quad (5)$$

so $F_H(T)$ becomes

$$F_H(T) = \frac{\int_{\Delta\lambda_H} [d\sigma_H(\lambda', \pi, T)/d\Omega]\xi(\lambda')d\lambda'}{[d\sigma_H(\pi)/d\Omega]\xi(\lambda_H)}. \quad (6)$$

A new function $F_H(T)$ has been introduced that carries all the temperature dependence of the lidar equation. It contains the effects of any changes in the lidar system's transmission efficiency, $\xi(\lambda)$, for wavelengths other than λ_H within passband $\Delta\lambda_H$. $\xi(\lambda_H)$ is the transmission efficiency at λ_H. The notation $d\sigma_H(\pi)/d\Omega$ is used to indicate the total Raman backscatter cross section for water vapor at the stimulating wavelength. For either the tripled Nd:YAG (354.7-nm) or the XeF excimer (351-nm) laser this value is approximately 6.2×10^{-34} m^2 sr^{-1},[34] and, at atmospheric temperatures, is essentially constant with temperature. In a typical lidar system, transmission changes that occur within the interval $\Delta\lambda_H$ are determined primarily by the interference filter itself, with smaller changes being contributed by other optics such as dichroic beam splitters. Although the transmission function that describes the passband of a lidar system is due to the character-istics of all optics that intercept the received signal, the interference filter by itself typically determines

Table 1. Values of the F_x Factor for Various Lidar Passband Widths (FWHM) and at Different Temperatures[a]

	Passband [ν_0(cm^{-1}), $\Delta\nu$(cm^{-1})]	Temperature (K)						Percent Change ($I_{200K}/I_{300K} \times 100$)
		200	220	240	260	280	300	
Narrow	Rayleigh (0, 24)	0.970	0.970	0.970	0.970	0.970	0.970	0.1
	Oxygen (1556, 21)	0.749	0.746	0.744	0.742	0.741	0.734	1.33
	Nitrogen (2331, 20)	0.851	0.850	0.850	0.850	0.848	0.848	0.39
	Water vapor (3654, 18)	0.961	0.950	0.938	0.926	0.913	0.900	6.7
Wide	Rayleigh (0, 159)	0.992	0.992	0.991	0.991	0.990	0.990	0.26
	Oxygen (1556, 142)	0.933	0.929	0.924	0.920	0.915	0.911	2.42
	Nitrogen (2331, 134)	0.947	0.944	0.940	0.938	0.935	0.931	1.61
	Water vapor (3654, 120)	0.997	0.995	0.993	0.992	0.990	0.988	0.9

[a]Widths are provided in wave numbers (cm^{-1}), corresponding to 0.3 nm (narrow) and 2.0 nm (wide) for each of the signals. The percentage change in the F_X factor (or equivalently the effective cross section) from 200 to 300 K is shown for each case as an indication of the temperature sensitivity for tropospheric measurements. Changes in the Rayleigh function F_R for a 24-cm^{-1}-wide passband occur in the fourth decimal place.

the majority of the transmission variation within the spectral band of interest. Thus in practice it may be more convenient to evaluate $\xi(\lambda')$ as a product of interference filter transmission, determined by use of a spectrophotometer device, and the transmission of the remaining optics, determined, for example, through the use of a calibrated lamp source or through atmospheric modeling.[35] The product $F_H(T)[d\sigma_H(\pi)/d\Omega]$ may be viewed as the effective molecular cross section that is consistent with the use of a monochromatic optical efficiency term $\xi(\lambda_H)$ in the lidar equation. Then the temperature dependence can be expressed as a simple multiplier of the normal Raman lidar equation. The situation is not so simple for the Rayleigh–Mie lidar equation, as is shown in Subsection 4.E below.

Data such as those presented in Fig. 1 may now be used to illustrate the calculation of $F_H(T)$ for a water-vapor measurement for which the 18-cm^{-1} (0.3-nm at 407.5 nm) FWHM passband also shown in the figure is used. Function $F_H(T)$ given in Eq. (6) may be determined by division of the values shown in Fig. 2 by the product of the total backscatter cross section $d\sigma_H(\pi)/d\Omega$ (inasmuch as Fig. 2 was generated by use of a peak lidar system transmission of 1.0). The results in the fourth line of Table 1 indicate that the effective cross section will be approximately 90–96% of the full Raman water-vapor OH-stretch cross section over the range of temperatures considered. By contrast (line eight in Table 1), the effective cross section differs from the full cross section by less than 1% when a 120-cm^{-1} passband is used for the water-vapor measurement. Similar calculations can be done for the Rayleigh (including the pure rotational Raman contribution) and the vibrational–rotational Raman signals from diatomic molecules.[23,27,37] Those results are also listed in Table 1 for passband widths in wave numbers that correspond to 0.3 nm (narrow) and 2 nm (wide) for the various signals excited at 354.7 nm. All passbands are assumed to be centered on their respective spectra. As listed in the table, the percent change in transmission between 200 and 300 K for each of these cases is as follows: Rayleigh 24- (159-) cm^{-1} passband, 0.09 (0.26)%; vibrational–rotational O_2 21- (142-) cm^{-1} passband, 1.3% (2.4%); vibrational–rotational N_2 20- (134-) cm^{-1} filter, 0.4% (1.6%). The effective cross section varies between 0.734 and 0.970 for the narrow cases considered and between 0.911 and 0.997 for the wide cases. These calculations illustrate that there are two ways in which the temperature dependence of F_X can influence Rayleigh–Mie and Raman lidar measurements. The first is due to the fact

Table 2. Conversion between Passbands Expressed in Wave Numbers and in Wavelengths at 354.7 or 532.1 cm

	Excitation Wavelength (nm)							
	354.7				532.1			
Molecule (Δcm^{-1})	Air (0)	O_2 (1556)	N_2 (2331)	H_2O (3654)	Air (0)	O_2 (1556)	N_2 (2331)	H_2O (3654)
Shifted wavelength (nm)	354.7	375.4	386.7	407.5	532.1	580.1	607.4	660.6
	Width (nm)							
Width (cm^{-1})								
25	0.31	0.35	0.37	0.42	0.71	0.84	0.92	1.09
50	0.63	0.70	0.75	0.83	1.42	1.68	1.85	2.18
100	1.26	1.41	1.50	1.66	2.83	3.37	3.69	4.37
150	1.89	2.13	2.24	2.49	4.25	5.05	5.54	6.55
200	2.52	2.82	2.99	3.32	5.67	6.74	7.39	8.74
250	3.15	3.52	3.74	4.15	7.09	8.42	9.24	10.9
300	3.77	4.23	4.49	4.98	8.50	10.1	11.08	13.1

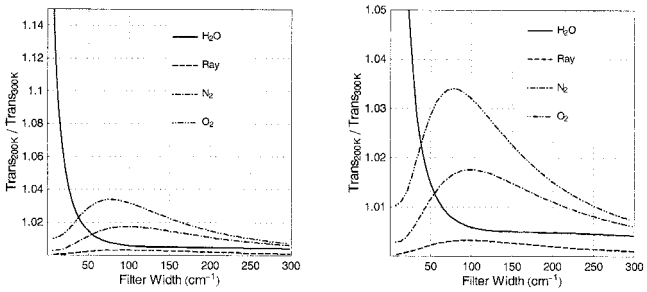

Fig. 3. Ratio of transmitted intensities at 200 and 300 K for Rayleigh and Raman (water-vapor, nitrogen, and oxygen) passbands for widths up to 300 cm^{-1} (~5 nm for excitation at 354.7 nm). The plot on the right presents the same data as on the left but with the vertical axis expanded for easier interpretation.

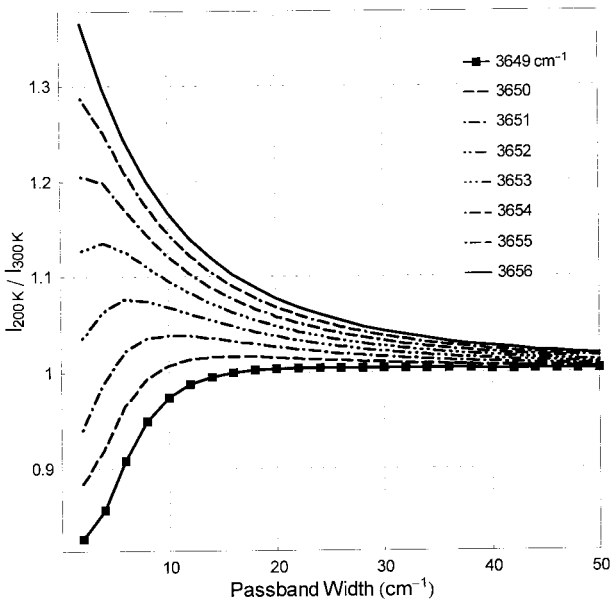

Fig. 4. Ratios of transmitted intensities between 200 and 300 K for water-vapor passbands of various widths and center positions. The center positions are given in the legend in units of wave numbers. Referring to Table 2, a passband width of 50 cm^{-1} corresponds to ~0.8 nm for excitation at 354.7 nm. The passband center positions in nanometers can be found in Table 3 at either 354.7 or 532.1 nm.

that F_X differs from unity, implying that the effective backscattering cross section is less than that used in the traditional lidar equations. The second is caused by the fact that F_X can change significantly as a function of temperature. This second effect implies that the calibration "constant" of the lidar system actually changes as a function of altitude due to changes in atmospheric temperature. Table 2 can be used for determining the corresponding passbands in nanometers for widths in inverse centimeters ranging from 25 to 300 for both doubled and tripled Nd:YAG excitation. For example, to span 50 cm^{-1} of the oxygen feature for excitation at 354.7 nm requires a filter of ~0.7 nm, whereas spanning the same wave-number range for excitation at 532.1 nm would require a filter width of ~1.7 nm.

Table 1 displays F_X calculated for bandwidths that correspond to 0.3 and 2.0 nm when they are excited at 354.7 nm, where the passband is assumed centered on the spectrum. It is interesting to consider other passband widths for the Rayleigh and three Raman signals. Figure 3 displays the percent change in F_X or, equivalently, in transmitted intensity, from 200 to 300 K [I (200 K)/I (300 K) × 100] as a function of passband width. The maximum percent change in transmitted Rayleigh signal is ~0.33% for a passband width of ~95 cm^{-1} (~1.2 nm at 354.7 and ~2.8 nm at 532 nm). There are much larger changes in the Raman vibrational signals. In particular, the temperature effect increases strongly in the water-vapor channel as the passband width decreases. For example, the ratio of transmitted intensities changes by more than 10% from 200 to 300 K for a passband width less than ~12 cm^{-1} (~0.2 nm at 407.5 nm). By contrast, the temperature sensitivity of diatomic molecules O_2 and N_2 decreases for passband widths less than ~75 cm^{-1} (~1 nm at 375.4 nm and ~2.5 nm at 580.4 nm) and ~100 cm^{-1} (~1.5 nm at 386.7 and ~3.7 nm at 607.8 nm), respectively, where peak percent changes of 3.3% and 1.8%, respectively, occur. These temperature changes reflect the fact that, for measurements of Raman vibrational spectra from diatomic molecules such as N_2 and O_2, as a passband that is centered on the q branch of the Raman feature becomes narrower, increasingly fewer of the vibrational–rotational lines will be transmitted, thus reducing the temperature-dependent effect.

Table 1 and Fig. 3 reveal a stronger temperature sensitivity for the water-vapor signal than for the other Raman signals. This results from the more complex, asymmetric nature of the water-vapor spectrum, as illustrated in Fig. 1. It is interesting to consider the effects of various combinations of water-vapor passband widths and center locations on the percent change in transmitted intensity from 200 to 300 K. Figure 4 shows the ratio of transmitted intensity for water-vapor passbands with FWHM up to 50 cm^{-1} (~1 nm at 407.5 nm) and central locations that vary from 3649 to 3656 cm^{-1} (407.45 to 407.56 nm). This figure reveals that the ratio of transmitted intensities is strongly dependent on the exact center location for the water-vapor passband. For example, the transmitted intensity of an 18-cm^{-1} (~0.3-nm) passband centered at 3656 cm^{-1} (407.56 nm) would change by ~8% from 200 to 300 K. If this passband is determined primarily by an interference filter, then tilting the filter by ~1° [assuming a filter's effective index of refraction of ~1.5 (Ref. 49)] to center it at 3649 cm^{-1} (407.43 nm) would essentially eliminate the temperature sensitivity. The total range of passband center location plotted in Fig. 3 is only 1.2 Å (1 Å = 0.1 nm) for excitation at 354.7 nm. This result indicates that one needs spectral transmission data with accuracy of ~0.1 Å to be able to assess the temperature dependence of narrowband water-vapor measurements with confidence.

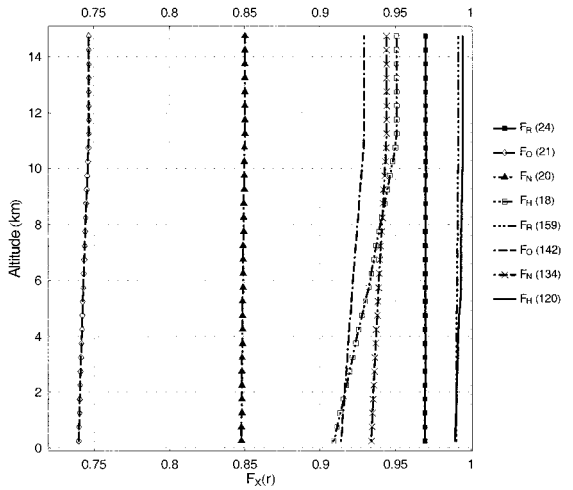

Fig. 5. Temperature-dependent functions $F_R(r)$, $F_O(r)$, $F_N(r)$, and $F_H(r)$ that are needed for evaluating the Rayleigh–Mie and Raman lidar equations plotted as functions of altitude, assuming a U.S. Standard Atmosphere temperature profile. The bandwidths (given parenthetically in units of inverse centimeters) correspond to 0.3 and 2.0 nm for excitation by 354.7-nm radiation.

D. Temperature-Dependent Functions versus Altitude

As an illustration of how to apply the temperature corrections, the profiles of $F_R(r)$, $F_N(r)$, $F_O(r)$, and $F_H(r)$ were evaluated, with the U.S. Standard Atmosphere[50] temperature profile and passband widths (in inverse centimeters) that correspond to 0.3 and 2.0 nm for excitation at 354.7 nm assumed. The results are presented in Fig. 5. Again, $F_X(r)\mathrm{d}\sigma_X(\pi)/\mathrm{d}\Omega$ quantifies the effective cross section for molecule X that is due to changes in transmission over the passband. The narrower passbands transmit less of the rotational or vibrational–rotational Raman lines and thus less of the total cross section. For O_2, the fraction of total cross section that is present in the vibrational–rotational lines is larger than for N_2, and thus, for comparable passband widths, $F_O(r)$ has a smaller value than $F_N(r)$.

E. New Formulation of the Single-Scattering Lidar Equations Containing Temperature Sensitivity

Using simplified formulations of the temperature sensitivity as in Eq. (6), one can now express the single-scattering Rayleigh–Mie and Raman lidar equations as follows:

$$P(\lambda_L, \Delta\lambda_R, r) = \frac{O_R(r)P_0(\lambda_L)A\xi(\lambda_L)\{F_R[T(r)]\beta_\pi^{\mathrm{mol}}(\lambda_L, r) + \beta_\pi^{\mathrm{aer}}(\lambda_L, r)\}}{r^2}\exp\left(-2\int_0^r \alpha(\lambda_L, r')\mathrm{d}r'\right), \quad (7)$$

$$P(\lambda_L, \Delta\lambda_X, r) = \frac{O_X(r)P_0(\lambda_L)A\xi(\lambda_X)F_X[T(r)]N_X(r)[\mathrm{d}\sigma_X(\pi)/\mathrm{d}\Omega]}{r^2}\exp\left\{-\int_0^r [\alpha(\lambda_L, r') + \alpha(\lambda_X, r')]\mathrm{d}r'\right\}, \quad (8)$$

where $\beta_\pi^{\mathrm{mol}}(\lambda_L, r) = N_R(r)\mathrm{d}\sigma_R(\pi)/\mathrm{d}\Omega$, $\mathrm{d}\sigma_R(\pi)/\mathrm{d}\Omega$ is the full molecular (Rayleigh) cross section, including the effects of rotational Raman scattering, and the passband transmissions are given by efficiency terms $\xi(\lambda_X)$. Notice that in the Rayleigh–Mie equation the temperature-dependent term $F_R[T(r)]$ multiplies only $\beta_\pi^{\mathrm{mol}}(\lambda_L, r)$ and not $\beta_\pi^{\mathrm{aer}}(\lambda_L, r)$ because only the molecular cross section exhibits the temperature dependence considered here. These forms of the lidar equations are used in the derivations that follow, after the calculation of the transmission terms in the lidar equations is carefully considered.

Table 3. Conversion Table for Center Positions of Water-Vapor Passbands

	Excitation Wavelength (nm)	
Shift (cm^{-1})	354.71	532.07
3649	407.45	660.25
3650	407.46	660.30
3651	407.48	660.34
3652	407.50	660.38
3653	407.51	660.43
3654	407.53	660.47
3655	407.55	660.52
3656	407.56	660.56

F. Atmospheric Transmission Function

The atmospheric transmission function for the Raman lidar equation, $\exp\{-\int_0^r [\alpha(\lambda_L, r') + \alpha(\lambda_X, r')]\mathrm{d}r'\}$, accounts for the fact that photons are transmitted into the atmosphere at laser wavelength λ_L and return at Raman-shifted wavelength λ_X for Raman species X. (One obtains the Rayleigh–Mie case simply by setting $X = L$.) The extinction that occurs at a certain wavelength is due, in general, to both scattering and absorption from both aerosols and molecules in the atmosphere and is a function of wavelength. The total extinction coefficient is therefore given by aerosol and molecular contributions:

$$\alpha(\lambda, r) = \alpha_{\mathrm{aer}}(r) + \sum_{i=1}^{M} N_i(r)[\sigma_i(\lambda) + \eta_i(\lambda)]. \quad (9)$$

In Eq. (9), $\alpha(\lambda, r)$ is the total extinction at wavelength λ and range r, $\alpha_{\mathrm{aer}}(r)$ is the extinction that is due to aerosol scattering and absorption, $N_i(r)$ is the molecular number density of the ith scattering–absorbing molecular species, $\sigma_i(\lambda)$ is the total scat-

tering cross section for the ith molecular species, and $\eta_i(\lambda)$ is the absorption cross section for the ith molecular species. M is the total number of molecular species being considered. The use of a XeCl excimer laser (~308 nm) as the output source requires the use of Eq. (9) because of significant ozone absorption of the outgoing beam in both the troposphere and the stratosphere.[51] For various other choices of output wavelength, molecular absorption is usually negligible. For example, for a Raman lidar that uses a UV laser such as a XeF excimer (~351-nm) or a frequency-tripled Nd:YAG (~355-nm) laser, the wavelength range of the return signals is approximately 350–410 nm, a region of the spectrum where molecular absorption is negligible.[52] The fundamental wavelength from the doubled Nd:YAG (~532-nm) and the Raman-shifted wavelengths for O_2 (~580 nm) and N_2 (~608 nm) also are not absorbed significantly below the stratosphere. However, measurements at these wavelengths through the stratospheric ozone layer are attenuated because of the presence of ozone by approximately 2–4% (tropospheric ozone absorption is negligible at these wavelengths owing to the much lower abundance of ozone in the troposphere than the stratosphere). The Raman-shifted wavelength for water vapor for excitation at ~532 nm is ~661 nm. Stratospheric ozone also absorbs at 661 nm by approximately 1–2%, but there is also weak absorption at this wavelength due to water vapor itself. For the standard tropical atmosphere of water vapor[50] the amount of absorption by water vapor of a signal at 661 nm is ~1%. For drier atmospheres the absorption will be less. Therefore, for Rayleigh–Mie or Raman measurements of O_2, N_2, and water vapor with a XeF excimer or tripled Nd:YAG lasers and for Rayleigh–Mie and Raman measurements of oxygen and nitrogen below the stratosphere with the doubled Nd:YAG laser, the molecular component of the atmospheric extinction coefficient $\alpha(\lambda, r)$ is due only to scattering by the various molecules in the atmosphere, and the following equation for the extinction coefficient applies:

$$\alpha(\lambda, r) = \alpha_{\text{aer}}(r) + \sum_{i=1}^{M} N_i(r)\sigma_i(\lambda). \tag{10}$$

Typical Rayleigh scattering formulas provide a composite cross section for the collection of molecules that make up normal air. Using this fact to reexpress the equation yields

$$\alpha(\lambda, r) = \alpha_{\text{aer}}(r) + N_{\text{air}}(r)\sigma_{\text{air}}(\lambda) \tag{11}$$

for the atmospheric extinction when absorption is not an issue. Equation (9) should be used to account for molecular absorption for the Raman lidar measurements discussed here when a 308-nm laser source is used or for measurements of water vapor or through the stratospheric ozone layer with an ~532-nm source, and for Raman water-vapor measurements with a doubled Nd:YAG laser (532 nm).

6. Atmospheric Extinction Caused by Molecules and Aerosols

To evaluate the atmospheric transmission function we need to evaluate separately the contributions that are due to molecular and aerosol extinction. The calculation of molecular extinction and optical depth, including the effects of the dispersion of polarization, has been thoroughly discussed elsewhere.[53,54] However, as some of the common formulas for Rayleigh extinction that are typically used in the lidar field[34] either do not account for depolarization at all or neglect its dispersion with wavelength, the calculation of molecular extinction is reviewed here first, after which the calculation of aerosol extinction is discussed.

A. Molecular Extinction and Backscattering Including the Effects of Polarization

In the absence of absorption, extinction of the laser beam is entirely due to scattering. Equations (12)–(14) are used for calculating the cross section per molecule for Rayleigh scattering[30,53,54]:

$$\sigma(\lambda) = \frac{24\pi^3[n_s^2(\lambda) - 1]^2}{\lambda^4 N_s^2 (n_s^2 + 2)^2} F_K(\lambda), \tag{12}$$

$$n_s(\lambda) = 10^{-8}\left[\frac{5791817}{238.0185 - (1/\lambda)^2} + \frac{167909}{57.362 - (1/\lambda)^2}\right] + 1, \tag{13}$$

$$F_K(\lambda) = \left[\frac{6 + 3\rho_0^t(\lambda)}{6 - 7\rho_0^t(\lambda)}\right], \tag{14}$$

where $\sigma(\lambda)$ is the cross section per molecule at wavelength λ; $n_s(\lambda)$ is an empirical formula[55] for the real refractive index for dry air at standard temperature and pressure (STP) at wavelengths greater than 230 nm (Ref. 54); N_s is the molecular number density for air at STP (2.547×10^{19} cm^{-3}); and $F_K(\lambda)$ is the King factor, shown defined in terms of ρ_0^t, the total (Rayleigh plus rotational Raman) depolarization from a natural light source,[30] the value of which is determined by the magnitudes of the parallel and perpendicular components of the dynamic polarizability,[53] $\alpha^{\parallel}(\lambda)$ and $\alpha^{\perp}(\lambda)$, as follows:

$$\rho_0^t(\lambda) = \frac{6\epsilon(\lambda)}{45 + 7\epsilon(\lambda)}, \tag{15}$$

$$\epsilon(\lambda) = 3\,\frac{\alpha^{\parallel}(\lambda) - \alpha^{\perp}(\lambda)}{\alpha^{\parallel}(\lambda) + 2\alpha^{\perp}(\lambda)}. \tag{16}$$

For example, $\rho_0^t(\lambda)$ changes from 0.0357 to 0.0273 over the range 250–1000 nm.[54] So it clear that the pertinent depolarization quantity ρ_0^t has a wavelength dependence that influences the Rayleigh scattering cross section. Also, owing to the random distribution of molecules in the atmosphere, the cross section given by Eq. (12) is valid regardless of laser polarization.

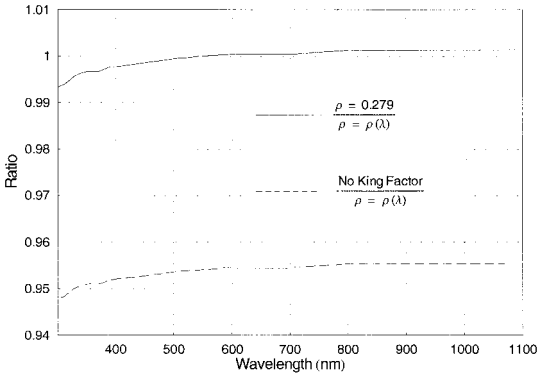

Fig. 6. Ratio of two approximate formulations of total Rayleigh scattering cross section, with the full treatment shown in Eq. (12) as a reference. The effect of using a constant depolarization is shown by a solid curve. The effect of neglecting the King factor completely is shown by a dashed curve. Significant errors are produced by use of either of the approximate methods.

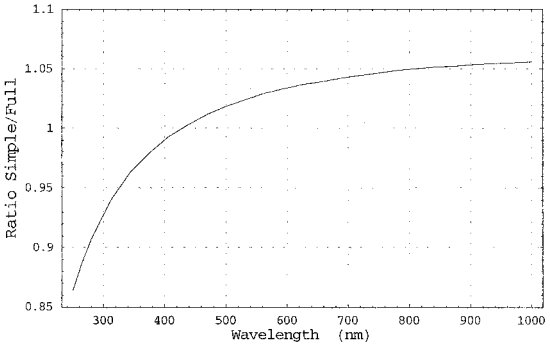

Fig. 7. Ratio of two formulations of the Rayleigh backscatter coefficient, given by Eqs. (19) and (21), plotted from 250 to 1000 nm. The difference between the simple numerical formula and Eq. (19) increases to more than 10% at short wavelengths.

1. *Comparison of Formulations of Rayleigh Cross Section*

The dispersion of depolarization must be included for an accurate determination of Rayleigh cross section as a function of wavelength.[54] Some calculations of Rayleigh cross section either neglect the dispersion of depolarization or omit the King factor completely.[34] Figure 6 compares these methods of calculating the Rayleigh cross section; it compares two approximate methods of calculating the Rayleigh cross section with the full calculation that uses Eq. (12). The first approximate calculation uses Eq. (12) but with a constant value for depolarization, chosen here to be 0.0279,[29] and the second method neglects the King factor completely. As the figure shows, including the dispersion of polarization changes the Rayleigh cross section by more than 1% across the wavelength range 250–800 nm compared with the wavelength-independent depolarization assumption. Neglecting the King factor yields a Rayleigh optical depth approximately 5% smaller than the actual value.

The total Rayleigh volume-scattering coefficient (in units of, for example, inverse meters) as a function of wavelength at STP is now given by[54]

$$\beta_s = N_s \sigma(\lambda). \tag{17}$$

For any pressure, temperature, or number density, the Rayleigh volume scattering coefficient may be determined from[54]

$$\beta^{\mathrm{mol}}(\lambda, r) = N(r)\sigma(\lambda) = \beta_s(\lambda)\frac{N(r)}{N_s} = \beta_s(\lambda)\frac{P(r)}{P_s}\frac{T_s}{T(r)}, \tag{18}$$

where β_s, P_s, and T_s are calculated at STP. In the absence of absorption, molecular extinction is determined completely by Rayleigh scattering, and thus the molecular component of the atmospheric extinction coefficient $\alpha(\lambda, r)$, from Eq. (11), is given by Eq. (18). The notation for the volume scattering coefficient, $\beta^{\mathrm{mol}}(\lambda, r)$, is not to be confused with the previously defined molecular backscatter coefficient, $\beta_\pi^{\mathrm{mol}}(\lambda, r)$. It is convenient at this point to describe the calculation of the Rayleigh backscatter coefficient.

2. *Calculation of Rayleigh Backscatter Coefficient*

To calculate the molecular (Rayleigh) backscatter coefficient one uses the following formulation[54]:

$$\beta_a^{\mathrm{mol}}(\theta, \lambda, r) = \frac{\beta^{\mathrm{mol}}(\lambda, r)}{4\pi} P_{\mathrm{Ray}}[\theta, \rho_0^t(\lambda)], \tag{19}$$

where $\beta_a^{\mathrm{mol}}(\theta, \lambda, r)$ is the Rayleigh angular volume scattering coefficient (in units of, for example, inverse kilometers per steradian). The backscattering case, of such special importance to lidar, has been given its own notation: $\beta_a^{\mathrm{mol}}(\pi, \lambda, r) = \beta_\pi^{\mathrm{mol}}(\lambda, r)$. Other than the 4π normalization factor, the right-hand side of this equation consists of two terms: $\beta^{\mathrm{mol}}(\lambda, r)$, the Rayleigh volume scattering coefficient given by Eq. (18), and $P_{\mathrm{Ray}}[\theta, \rho_0^t(\lambda)]$, the scattering amplitude as a function of angle, which is equal to[56]

$$P_{\mathrm{Ray}}[\theta, \rho_0^t(\lambda)] = \frac{3}{2[2 + \rho_0^t(\lambda)]}\{[1 + \rho_0^t(\lambda)] + [1 - \rho_0^t(\lambda)]\cos^2\theta\}, \tag{20}$$

where $\rho_0^t(\lambda)$ is the Rayleigh depolarization factor defined above. One obtains the Rayleigh backscattering coefficient simply by setting $\theta = \pi$ in Eqs. (19) and (20). The formulation of the Rayleigh scattering phase function given in Eq. (20) is from Goody and Yung[56] and is in fact equivalent to the form given by Chandrasekhar[57] and Bucholtz.[54] However, the Goody–Yung form is expressed directly in terms of the depolarization of natural light, $\rho_0^t(\lambda)$, that appears in the King factor, as opposed to a term that Chandrasekhar and Bucholtz refer to as $\gamma(\lambda) = \rho_0^t(\lambda)/[2 - \rho_0^t(\lambda)]$, which is equivalent to the term $\rho_v^t(\lambda)$ defined by Young[29] as the depolarization of incident light polarized normal to the scattering plane.

It is interesting to compare the formulation of the

Rayleigh backscattering coefficient in Eq. (19) to a simpler numerical version that is common in the lidar literature but that does not account for the effects of the dispersion of depolarization. The simpler equation is[34]

$$\beta_{\pi}^{\text{simpler}}(N, \lambda) = N5.45\left[\frac{550}{\lambda(\text{nm})}\right]^4 \times 10^{-28}\ (\text{cm}^{-1}\ \text{sr}^{-1}), \tag{21}$$

where N is the molecular number density in units of cm^{-3} inverse cubic centimeters. Figure 7 shows the ratio of Eqs. (21) and (19) over a range of 250–1000 nm, where the latter equation has been evaluated at an angle of π.

The two methods differ by more than 10% for wavelengths shorter than approximately 280 nm and by more than 5% for wavelengths greater than approximately 800 nm. Near 350 nm, where the popular Raman lidar laser sources of the tripled Nd:YAG and the XeF excimer lasers have their output, the simpler formulation is ~3% smaller than the full treatment given in Eq. (19), whereas, in the vicinity of 530 nm, the approximate wavelength of the Nd:YAG laser, the simpler treatment is now ~3% larger. These are significant differences, implying that the complete formulation of the Rayleigh backscatter coefficient given by Eq. (19) should be used instead of simpler formulations such as that in Eq. (21).

B. Aerosol Extinction

To compute aerosol extinction analytically generally requires knowledge of the exact nature of the aerosols that are responsible for the extinction. Given the size distribution of the aerosols as a function of range and both real and imaginary indices of refraction, a calculation that uses Mie theory can be performed that will estimate the extinction as a function of range. This can be done accurately for nonprecipitating cloud water droplets, which are spherical, provided that multiple scattering is not significant. But for other aerosols, which can have irregular shapes that are usually not known, calculations of aerosol scattering properties by use of Mie theory are approximations at best.

However, with the Raman lidar, another approach to the calculation of aerosol extinction is possible. One may use the Raman vibrational[58] (or the pure rotational[39]) signal from nitrogen or oxygen to calculate the round-trip atmospheric extinction, which for vibrational Raman scattering occurs at the laser wavelength for the outgoing path and at the Raman-shifted wavelength for the return path.

1. Development of the Extinction Equations Including the Effects of Temperature Sensitivity

Aerosol extinction is typically quantified by use of Raman lidar by measuring the vibrational scattering from N_2 or O_2.[9,58] At the UV and visible wavelengths of the lasers that are typically used in Raman lidar systems, atmospheric absorption is negligible, as discussed earlier, so aerosol extinction is determined by the total amount of light scattered into all directions. This is the integral of the aerosol scattering intensity as a function of angle (the phase function) and quantifies an important radiative property of the aerosols. The equation for calculating aerosol extinction by use of the temperature-dependent Raman lidar data can be derived along lines similar to those of Ansmann *et al.*[58] Assuming the use of the Raman N_2 signal for the calculation of aerosol extinction, the result is

$$\alpha_{\text{aer}}(\lambda_L, r) + \alpha_{\text{aer}}(\lambda_N, r) = \frac{\text{d}}{\text{d}r}\left(\ln\left\{\frac{O_N(r) F_N[T(r)] N_N(r)}{r^2 P(\lambda_N, r)}\right\}\right) - \alpha_{\text{mol}}(\lambda_L, r) - \alpha_{\text{mol}}(\lambda_N, r), \tag{22}$$

where $\alpha_{\text{aer}}(\lambda_L, r)$ is the extinction that is due to aerosols on the outgoing path at the laser wavelength, $\alpha_{\text{aer}}(\lambda_N, r)$ is the aerosol extinction on the return path at the Raman-shifted wavelength, $\alpha_{\text{mol}}(\lambda_L, r)$ is the molecular extinction at the laser wavelength, and $\alpha_{\text{mol}}(\lambda_N, r)$ is the molecular extinction at the Raman-shifted wavelength.

Equation (22) is the fundamental Raman lidar aerosol extinction equation. It is identical to the results of Ansmann *et al.*,[58] except for the inclusion of the temperature-dependent factor $F_N[T(r)]$. The atmospheric number density is required for evaluation of this equation both for calculation of the molecular extinction terms [through the use of Eq. (18)] as well as for evaluating the number density $N_N(r)$. In the lowest ~100 km of the atmosphere the total atmospheric density is proportional to $N_N(r)$ and thus its use gives identical results in the equation. The sensitivity of Raman measurements of aerosol extinction to changes in atmospheric temperature and density variations has been studied by Ansmann *et al.*[58] Their conclusion was that the use of a standard atmospheric model for calculating molecular extinction can introduce significant errors in aerosol extinction when the aerosol loading is low. Therefore the more accurate molecular number density profile available from a radiosonde is recommended under such conditions.

Equation (22) indicates that the fundamental quantity that can be evaluated with a Raman lidar is the two-way extinction that occurs along the round-trip path from the laser to a scattering element and back to the telescope. To translate this two-way extinction into one-way extinction at a single wavelength requires knowledge of the wavelength scaling

of aerosol extinction. The scaling of aerosol extinction may be handled as follows[59]:

$$\frac{\alpha_{\mathrm{aer}}(\lambda_L, r)}{\alpha_{\mathrm{aer}}(\lambda_N, r)} = \left(\frac{\lambda_N}{\lambda_L}\right)^{k(r)}, \tag{23}$$

where $k(r)$ may vary approximately from 0 to 2, depending on the nature of the aerosols,[9] and is a function of range. With Eq. (23) the expression for aerosol extinction at the laser wavelength becomes

$$\alpha_{\mathrm{aer}}(\lambda_L, r) = \frac{(\mathrm{d}/\mathrm{d}r)[\ln\{O_N(r)F_N[T(r)]N_N(r)/r^2P(\lambda_N, r)\}] - \alpha_{\mathrm{mol}}(\lambda_L, r) - \alpha_{\mathrm{mol}}(\lambda_N, r)}{1 + (\lambda_L/\lambda_N)^{k(r)}}. \tag{24}$$

An alternative form of Eq. (24), which is preferred because it allows quantities to retain their original statistical distributions when the numerical derivative is determined,[60] is

$$\alpha_{\mathrm{aer}}(\lambda_L, r) = \frac{\dfrac{1}{O_N(r)}(\mathrm{d}/\mathrm{d}r)O_N(r) + [1/F_N(T)](\mathrm{d}/\mathrm{d}r)F_N[T(r)] + [1/N_N(r)](\mathrm{d}/\mathrm{d}r)N_N(r) - \dfrac{1}{r^2P(\lambda_N, r)}\mathrm{d}/\mathrm{d}r[r^2P(\lambda_N, r)] - \alpha_{\mathrm{mol}}(\lambda_L, r) - \alpha_{\mathrm{mol}}(\lambda_N, r)}{1 + (\lambda_L/\lambda_N)^{k(r)}}. \tag{25}$$

As described in Ref. 60, the evaluation of the derivative term in Eq. (24) or Eq. (25) through the use of the technique of least-squares fitting assumes the data to be regressed are normally distributed. The application of least-squares fitting to Eq. (24) therefore violates one of the assumptions of the technique and should be avoided. The use of Eq. (25) permits all quantities that are being regressed to retain their original statistical distributions, which are assumed to be Gaussian or near Gaussian. Equation (25), therefore, is preferred to Eq. (24) for evaluating aerosol extinction because the ratio of two Gaussian distributed quantities is not Gaussian.

In principle, Eq. (25) can be used over the entire range of the lidar profile for evaluating the aerosol extinction. However, in practice it is quite difficult to quantify the lidar channel overlap function sufficiently well that Eq. (25) can be applied in the overlap region. This is so because the derivative of the overlap must be evaluated. In the overlap region, the signal may be changing rapidly, so small errors in quantifying the overlap function can introduce large errors in the derived aerosol extinction. For this reason calculations of aerosol extinction are typically performed on the portion of the lidar profile that is fully overlapped, i.e., where $O_N(r) = 1$. It should be noted as well that, inasmuch as the extinction will typically be evaluated over relatively short ranges (i.e., dr will in general be of the order of 100 m), the factor $F_N[T(r)]$ will have little influence because, as can be seen from Fig. 5, its change is insignificant over such short ranges. This is the case in the normal atmosphere because $F_N[T(r)]$ is not a strong function of range; for measurements of extinction in a smokestack or in the vicinity of flames it will not be the case, however, and the factor $F_N[T(r)]$ could change over short ranges and influence the extinction calculation.

Before Eq. (25) is evaluated for tropospheric aerosols, the possible influence of multiple scattering on these measurements must be addressed. Tropospheric aerosols, excluding cloud particles, range in size from less than 0.1 μm in radius to 10 μm and larger in some cases.[61] The multiple scattering that is due to aerosols in this size range is studied in Appendix A. The simulations performed there indicate that multiple scattering is likely to be negligible for

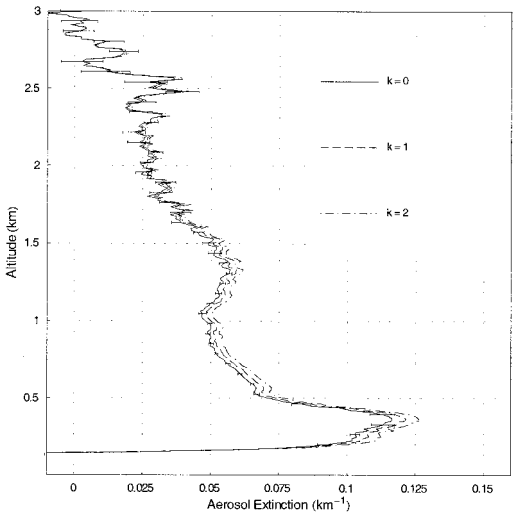

Fig. 8. Aerosol extinction (at 351 nm) calculated from a 20-min summation of data from the night of 26 August 1998 at Andros Island, Bahamas. The sensitivity of the aerosol scaling parameter, k, is tested here.

boundary layer extinction measurements. However, for elevated desert dust layers multiple scattering may have a small but noticeable effect on the calculation of extinction.

2. Example Aerosol Extinction Profile

An example of aerosol extinction computed from data acquired by the NASA/Goddard Space Flight Center Scanning Raman Lidar (SRL) during the third Convection and Moisture Experiment[8] (CAMEX-3) on the night of 26 August 1998 at Andros Island, Bahamas, is shown in Fig. 8. At the time of this field campaign the SRL used a XeF excimer laser (351 nm), a 0.76-m telescope, and high- and low-range photomultiplier tubes for each of the Rayleigh–Mie, O_2, N_2, and water-vapor signals.[5] The results shown were obtained from the raw Raman lidar measurement of molecular nitrogen by correction for the finite photon counting bandwidth, subtraction of the background, and then application of Eq. (25). For reference, various photon counting correction techniques are reviewed in Appendix B.

The aerosol extinction profiles shown use a 20-min summation of data. The molecular extinction coefficients were derived from Eq. (18) and the atmospheric density that was measured by a radiosonde launched that night. In the figure, the influence of the aerosol scaling parameter k (known as the Angstrom coefficient) is also tested. Figure 8 shows a typical aerosol profile from Andros Island during the CAMEX-3 campaign. The values of extinction below ~0.25 km are influenced by the lidar overlap function. Changing the Angstrom coefficient (considered constant with range) from $k = 0$ to $k = 2$ increases the aerosol extinction values by approximately 8%. It has the same effect on the aerosol optical depth between the altitudes of 0.25 and 3.0 km, which one may calculate by simply integrating the extinction curve over this altitude range. For $k = 1$, the aerosol optical thickness (at 351 nm) from 0.25 to 3 km was approximately 0.13 for this example.

The uncertainty in the Angstrom coefficient can be reduced by use of coincident sunphotometer data, although the sunphotometer provides only a column average value, whereas the lidar is measuring the profile of aerosols. The uncertainty in the Angstrom coefficient determined with a sunphotometer is a function of the wavelength interval used to determine the coefficient, the aerosol optical depth, and the quality of the calibration of the instrument in use. In general, for instruments in the NASA/Goddard Space Flight Center AERONET network (http://aeronet.gsfc.nasa.gov:8080/), the uncertainty of the Angstrom coefficient will be less than ±0.2 for the 340–380-nm wavelength interval if the aerosol optical thickness is greater than 0.4.[62,63] It is interesting to note that because of the existence of the AERONET reference standard at the NASA/Goddard Space Flight Center a ±0.2 uncertainty in Angstrom coefficient is obtained for measurements made there when aerosol optical depths are greater than 0.2.[64] It is estimated that an uncertainty in the value of $k(r)$ contributes an error of less than 5% to the aerosol extinction measurements shown in Fig. 8.

An aerosol optical depth of ~0.13 in the current example implies that approximately 12% of the light was scattered from the beam by aerosols ($e^{-0.13} \cong 0.88$). These measured values of aerosol extinction in the UV can be used to estimate the horizontal visibility experienced by ground-based observers. The visual range may be estimated from the empirical formula[34]

$$\alpha(\lambda) \approx \frac{3.91}{R_v}\left[\frac{550}{\lambda(\mathrm{nm})}\right]^k [\mathrm{km}^{-1}], \tag{26}$$

where α is the total atmospheric extinction coefficient and R_v is the visual range. At visible wavelengths and under most aerosol loading conditions, aerosol extinction is the dominant source of atmospheric attenuation.[34] For example, near the surface in Fig. 8, aerosol extinction at 351 nm was approximately 0.1 km^{-1}. By contrast, molecular extinction under conditions of STP and for Eq. (17) is approximately 0.01 km^{-1}. Using these values in Eq. (26) yields a value of visual range in excess of 50 km. The aerosol loading that was present on 26 August was typical for Andros Island during the CAMEX-3 campaign, implying that aerosol optical depths were low and visibilities were generally good.

This example demonstrates that the aerosol optical depth is an important parameter than influences visibility and thus radiative transfer. As demonstrated above, the optical depth can be determined by integration of the aerosol extinction profile. When the optical depth is calculated in this manner, however, errors at all levels in the extinction profile must be added together to yield the error budget for calculation of the optical depth. This can result in a larger uncertainty in the determination of the optical depth than the more straightforward calculation that now is presented.

4. Aerosol Optical Depth

Integrating both sides of Eq. (22) over the range $\{r_1, r_2\}$ yields the two-way aerosol optical depth between r_1 and r_2:

$$\int_{r_1}^{r_2} [\alpha(\lambda_L, r) + \alpha(\lambda_N, r)]\mathrm{d}r = \left(\ln\left\{\frac{O_N(r)F_N[T(r)]N_N(r)}{r^2P(\lambda_N, r)}\right\}\right)_{r_1}^{r_2} - \int_{r_1}^{r_2} [\alpha_{\mathrm{mol}}(\lambda_L, r) + \alpha_{\mathrm{mol}}(\lambda_N, r)]\mathrm{d}r$$

$$= \ln\left\{\frac{O_N(r_2)F_N[T(r_2)]N_N(r_2)r_1^2P(\lambda_N, r_1)}{O_N(r_1)F_N[T(r_1)]N_N(r_1)r_2^2P(\lambda_N, r_2)}\right\} - \int_{r_1}^{r_2} [\alpha_{\mathrm{mol}}(\lambda_L, r) + \alpha_{\mathrm{mol}}(\lambda_N, r)]\mathrm{d}r. \tag{27}$$

The use of Eq. (27) to calculate aerosol optical depth eliminates the need to perform a derivative of the lidar signal. This simplifies calculations when all that is needed is the mean value of extinction through a layer such as is required for calculating the optical depth of the layer.

The error in the aerosol optical depth has both random and systematic components. It is in general difficult to evaluate the systematic part of the error because knowledge of the absolute value of the quantity being measured is required. However, because the values of density and temperature that one uses in the evaluation of Eq. (27) would likely come from a single model profile or radiosonde measurement, there is likely to be a systematic component to the errors in $F_N[T(r)]$, $N_N(r)$, and $\alpha_{\text{mol}}(\lambda_L, r)$. It is clear from Eq. (27) that the systematic component of errors in $F_N[T(r)]$ and $N_N(r)$ will tend to cancel because of the ratio inside the logarithm. However, a systematic error in density of a certain percent will have the same percent effect on the calculated molecular optical depth. As mentioned above, this effect was considered by Ansmann *et al.*[58]; they concluded that radiosonde measurements of density would be preferred over model values in the evaluation of Eq. (27) for small aerosol optical depths.

The random component of the error in optical depth may be calculated from standard error propagation formulas[65] and is given by

$$\sigma^2_{\text{AerosolOD}} \simeq \frac{\sigma^2_{O_N(r_2)}}{O^2_N(r_2)} + \frac{\sigma^2_{O_N(r_1)}}{O^2_N(r_1)} + \frac{\sigma^2_{F_N}[T(r_2)]}{F^2_N[T(r_2)]} + \frac{\sigma^2_{F_N}[T(r_1)]}{F^2_N[T(r_1)]} + \frac{\sigma^2_{N_N(r_2)}}{N^2_N(r_2)} + \frac{\sigma^2_{N_N(r_1)}}{N^2_N(r_1)} + \frac{\sigma^2_{P(\lambda_N, r_2)}}{P^2(\lambda_N, r_2)} + \frac{\sigma^2_{P(\lambda_N, r_1)}}{P^2(\lambda_N, r_1)} + 2\sigma^2_{\text{MolecularOD}}, \quad (28)$$

where, to be clear, $\sigma^2_{\text{AerosolOD}}$ refers to the variance of the two-way aerosol optical depth and $\sigma^2_{\text{MolecularOD}}$ refers to the variance of the one-way molecular optical depth. If $F_N[T(r)]$ varies little over the range of the optical depth calculations, such as in the normal atmosphere, it should contribute at most a small amount to the total error. In a smokestack or in flames, however, the temperature can change significantly over short ranges. Thus $F_N[T(r)]$ can be considered negligible over ranges where the temperature does not change appreciably. Therefore, if the temperature changes slowly over the range that is being considered and, furthermore, if the calculation is done outside the region where the overlap function is an influence, the error equation reduces to

$$\sigma^2_{\text{AerosolOD}} \simeq \frac{\sigma^2_{N_N(r_2)}}{N^2_N(r_2)} + \frac{\sigma^2_{N_N(r_1)}}{N^2_N(r_1)} + \frac{\sigma^2_{P(\lambda_N, r_2)}}{P^2(\lambda_N, r_2)} + \frac{\sigma^2_{P(\lambda_N, r_1)}}{P^2(\lambda_N, r_1)} + 2\sigma^2_{\text{MolecularOD}}. \quad (29)$$

The error in the radiosonde density data will determine the error budget for three of the terms above. Also, for a lidar system such as the SRL that uses photon counting data acquisition, Poisson statistics apply, so the variance in a measurement equals the accumulated number of counts of the measurement itself. Putting these results together yields

$$\sigma^2_{\text{AerosolOD}} \simeq \frac{1}{P(\lambda_N, r_2)} + \frac{1}{P(\lambda_N, r_1)} + 4\ \text{RadErr}^2, \quad (30)$$

where RadErr indicates the fractional random error in the radiosonde density measurement.

The equations are now developed for the two-way particle optical depth. If one desires to determine the one-way particle optical depth, it is necessary to use Eq. (23) to handle the wavelength scaling. The appropriate error equation is this case is approximately one half of relation (30), depending on the value of $k(r)$ used in Eq. (23). This completes the description of numerous calculations required for evaluating the lidar equation. Now one may derive the meteorological quantities of water-vapor mixing ratio, aerosol scattering ratio, aerosol backscatter coefficient, and aerosal extinction-to-backscatter ratio by considering ratios of Raman lidar signals. This issue is addressed in part 2 of this series.[28]

7. Summary

As the number of Raman water-vapor and aerosol lidar systems in use in the world has been increasing recently, particularly in Europe, it seems an appropriate time to undertake an updated evaluation of the traditional Raman lidar technique for measuring water-vapor and aerosols, including effects such as the temperature dependence of Raman scattering. Toward that end, this paper is part one of a thorough two-part review of the traditional, single-laser-wavelength Raman lidar technique for measuring atmospheric water vapor and aerosols. In this paper, a detailed study of the evaluation of both the Rayleigh–Mie and the Raman lidar equations has been presented, including the effect of the temperature sensitivity of both rotational and vibrational–rotational Raman scattering. New forms of the Rayleigh–Mie and Raman lidar equations were developed that permit the temperature sensitivity of these equations to be confined to a single term that in the case of the Raman lidar equation becomes a multiplier of the traditional equation. These temperature-dependent factors were calculated for Rayleigh, Raman N_2, O_2, and water-vapor signals by use of different passband widths and center positions. The Raman water-vapor simulations were performed with use of recent results that permit the full OH-stretch mode of water vapor to be simulated. The effects of the temperature sensitivity of Raman scattering on the Rayleigh–Mie and Raman lidar measurements considered here are of two general types: 1) an effective molecular cross section (whether Rayleigh or Raman) that is less than the full cross section and 2) given that temperature is a function of alti-

tude, a change in the sensitivity of the lidar system as a function of altitude due to changes in the intensities of individual (temperature-dependent) spectral lines. The effective cross sections were reduced more for the narrow passbands (~0.3 nm) considered here, with results ranging from 0.97 (Rayleigh) to 0.73 (Raman O_2), than for the wide passbands (2.0 nm), where results ranged from 0.99 (Rayleigh–Mie) to 0.91 (Raman O_2). The change in the sensitivity as a function of altitude was also in general larger for narrow passbands than for wide passbands. The water-vapor signal demonstrated the largest height-dependent effects, with changes of more than 6% in sensitivity for the narrow passband case simulated. By contrast, the effective Rayleigh cross sections were nearly height independent for both narrow and wide passbands. The calculation of atmospheric transmission was discussed in detail. Differences of as much as 5% were found in calculations of molecular extinction owing to the effects of the dispersion of depolarization. A simple formulation of Rayleigh backscattering that is commonly used in the lidar field was found to differ significantly from the full calculations that are suggested here. Temperature-dependent aerosol extinction and optical depth equations were presented. The influence of the wavelength scaling of aerosols was considered in these calculations. In appendixes the influence of multiple scattering was considered for boundary layer and elevated aerosol layers. It was found that multiple scattering owing to elevated dust layers can significantly affect the calculation of extinction when certain lidar configurations are used. Correction techniques for photon counting pulse pileup were reviewed. In part 2,[28] the temperature-dependent equations developed here are used to derive new forms of the ratio equations for Raman lidar water-vapor and aerosol analysis.

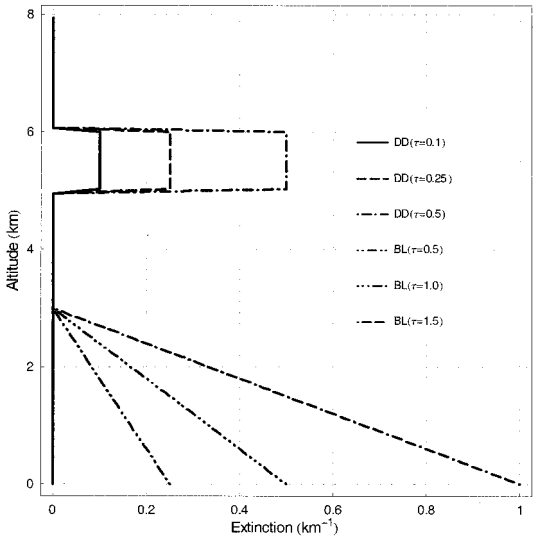

Fig. 9. Six synthetic aerosol extinction profiles created to test the influence of multiple scattering on measurements of aerosol extinction. Three are for use in the simulations of elevated dust layers; the other three are for simulation of boundary layer aerosols. The desert dust profiles are labeled DD(τ), where τ is the optical depth of the layer. The corresponding key for the boundary layer aerosols is BL.

Appendix A: Influence of Multiple Scattering on Tropospheric Aerosol Extinction Measurements

1. Introduction

For light scattered by particles of the same dimension as or larger than the wavelength of the incoming light, as the particle size increases, forward-scattered light is confined to an increasingly narrow angular cone. This makes it more likely that a photon that is scattered forward in a first scattering event will interact with another particle in a second scattering event and be backscattered within the field of view of the lidar receiver.

The lidar equations formulated above were for single scattering only. Therefore, in the case of scattering involving large particles, for which multiple scattering is more likely to occur, the use of the single-scattering equations can lead to errors in the calculated quantities. Most of the quantities derived from Raman lidar data are based on ratios of lidar signals, so the multiple scattering influence tends to cancel in the ratio.[66] Examples of these quantities are the water-vapor mixing ratio, the liquid water mixing ratio, the aerosol scattering ratio, and the aerosol backscatter coefficient. However, aerosol extinction and optical depth are calculated from only a single lidar signal (e.g., Raman nitrogen), which, in the case of large particles, can be significantly influenced by multiple scattering.

The influence of multiple scattering on lidar signals is related to the optical depth of the scattering medium, the sizes of particles that are doing the scattering, the range to the scattering volume, the laser divergence, and the telescope's field of view. We use the formulation developed by Eloranta[67] here to study this influence, assuming 1-mrad laser divergence and 2-mrad telescope field of view. A description of the equations used here was published recently for Raman lidar measurements of cirrus cloud multiple scattering.[8] It is important to note that the modeling of multiple scattering for the molecular (as opposed to the Rayleigh–Mie) signal is aided by the slowly varying nature of the molecular phase function in the backscatter direction.[67] By contrast, to simulate multiple scattering for the Rayleigh–Mie signal requires a knowledge of the profile of particle size because the Mie phase function changes rapidly near the exact backward direction.

2. Multiple Scattering by Tropospheric Aerosols: Boundary Layer and Elevated Dust Layers

Six synthetic profiles of aerosol extinction were created for a study of the influence of multiple scattering on the measurement of extinction by use of Raman lidar and are shown in Fig. 9. The boundary layer extinction profiles have aerosol optical depths of 0.375, 0.75, and 1.5, respectively, to simulate low,

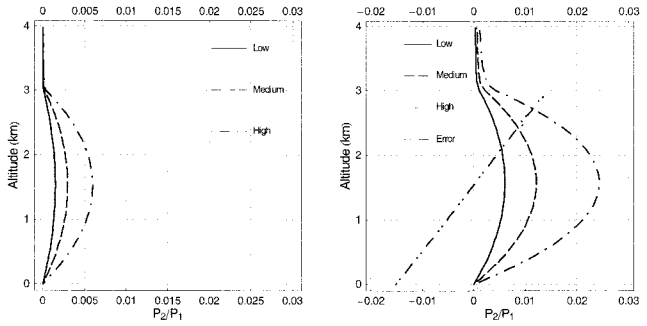

Fig. 10. Multiple scattering simulations for the boundary layer aerosol profiles shown in Fig. 9. Calculations with constant size aerosols assumed to be of 0.5-μm radius are shown at the left and of 2.0 μm radius are shown at the right. The error in extinction is plotted for high optical depth at the right.

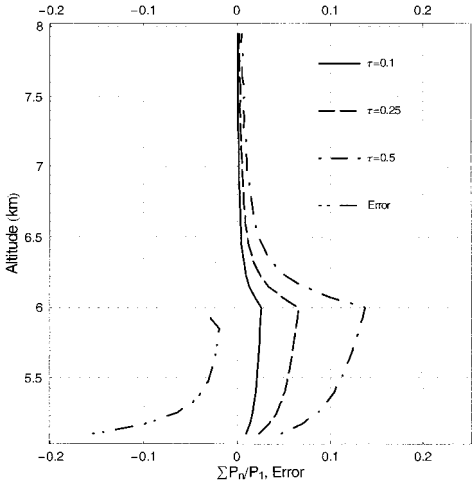

Fig. 11. Multiple scattering simulations for a layer of desert dust at 5–6 km. The mean particle size used is 3 μm, and three optical depths studied are 0.1, 0.25, and 0.5. The error in extinction is also plotted for the 0.5-optical depth case.

medium, and high aerosol loading. The extinction profiles simulating elevated dust layers are 1 km thick with bases located at an altitude of 5 km. The layers have optical depths of 0.1, 0.2, and 0.5.

Aerosols can range in size from much less than 1 μm (rural aerosols) to more than 10 μm (desert dust). Second-order multiple scattering was calculated for the three boundary layer extinction profiles shown in Fig. 9; it was assumed that the aerosol particles were of constant radius throughout the profile where the radii chosen were 0.5 and 2.0 μm. The results are shown in Fig. 10, with the 0.5-μm calculations at the left and the 2.0-μm calculations at the right. The plot of the 2.0-μm results also includes the fractional error in the extinction as a function of range for the 0.5 optical depth case.

The multiple scattering that is due to 0.5-μm aerosols is considerably smaller than that for the 2-μm aerosol. Considering the 2-μm results shown at the right, one can see that at the peak of the multiple scattering for the 0.5 optical thickness case, the second-order multiple scattering is less than 3% of the single scattering. The error in extinction that is due to second-order multiple scattering is also plotted for the case of high optical depth. The negative error is largest, with a value of $\sim -1.5\%$ at the surface where the aerosol layer is first encountered. It then increases toward zero at an altitude of ~1.5 km, where the slope of the P_2/P_1 curve is zero. Above this altitude until the top of the aerosol layer, the error is positive, reaching a maximum positive value of ~1.5% at the top of the layer. Because the optical depth is just the integral of extinction, the error in optical depth that is due to second-order multiple scattering will be at most 1.5% as well. Third-order scattering will be insignificant because of its much lower probability than second-order scattering.

The U.S. Air Force Geophysics Laboratory's marine oceanic aerosol model[61] peaks at 0.3 μm and predicts that there will be only 51% and 1.8% as many particles of radii 0.5 and 2 μm, respectively, as at the peak. For particles larger than 2 μm, the abundance drops exponentially. Therefore, because of the relative lack of large particles that these model calculations predict for tropospheric aerosols and the generally small effect that multiple scattering has on the calculation of boundary layer aerosol extinction, multiple scattering is unlikely to present a significant error source for boundary layer aerosols.

The same may not be the case for elevated layers of desert dust, which have been observed at large distances from their source regions[68–71] and are characterized by preferential population of the coarse mode part of the distribution.[72] With other parameters fixed, if the range to the scattering medium is increased the observed multiple scattering increases as well. This is so because a larger geometrical area is observed by a fixed-field-of-view telescope as the range increases. Therefore one might expect that an elevated layer of aerosols would exhibit more multiple scattering than the same layer at lower altitudes. Furthermore, Dubovik *et al.*[72] reported aerosol mean radii of $\sim 2.5 \pm 0.6$ μm for sunphotometer measurements of desert dust made over a period of approximately 2 years in Bahrain. Therefore, to illustrate the possible influence of multiple scattering on extinction measurements of elevated desert layers, Fig. 11 shows multiple scattering calculations for a 1-km-thick dust layer at 5–6 km with optical depths of 0.1, 0.25, and 0.5 for the elevated extinction profiles shown in Fig. 9. The aerosol size simulated is 3 μm. Both second- and third-order multiple scattering was used in these simulations. The error in extinction that is due to multiple scattering is also plotted for the 0.5-optical depth case. The figure shows that the peak ratios of multiple scattering to single scattering for the three optical depths are ~0.03, 0.07, and 0.14. The error in extinction for 0.5 optical depth is maximum and negative, with a value of ~15% at the base of the aerosol layer. The error in extinction for 0.25 optical depth (not plotted) is approximately half of that for 0.5 optical depth, or ~7%

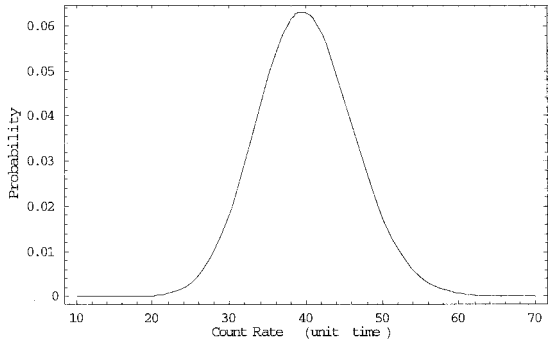

Fig. 12. Probability of measuring n counts for a Poisson process characterized by a mean count rate of 40 counts per unit of time.

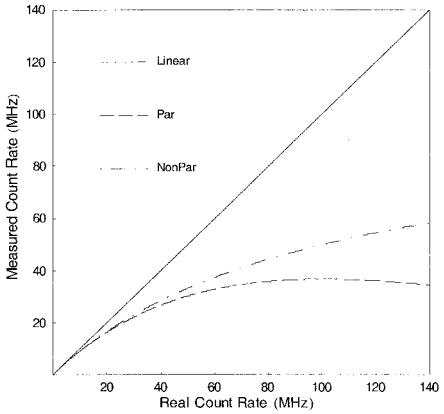

Fig. 13. Comparison of paralyzable and nonparalyzable count corrections by use of a resolving time of 10 ns. The observed count rate of a paralyzable system tends toward zero with increasing true count rate. The observed count rate of a nonparalyzable system tends toward the maximum count rate as the real count rate increases. A perfect linear system is also represented.

at the base. The error in extinction approaches zero at the top of the elevated layer. Above the layer, where the influence of multiple scattering can still be seen, the derived aerosol extinction will be nonzero, where in fact there are no aerosols. Therefore the error in extinction is essentially infinite. This is an example of the phenomenon known as pulse stretching that can be a significant issue for space-based lidar systems because of the enhancement of multiple scattering created by the large distance from the lidar system to the extinguishing layer. The difference in the behavior of the error in extinction versus range between the boundary layer cases shown above and the elevated layers shown here are due mainly to the different profiles of extinction assumed. The conclusion based on this figure is that multiple scattering can become a significant error source in the calculation of extinction in elevated layers of desert dust.

Appendix B: Photon Pileup Correction

Raman lidar systems frequently make use of photon counting data acquisition systems because of the weak nature of Raman scattering. For example, all the data acquired by the SRL during the CAMEX-3 field campaign used photon counting electronics. Photon counting electronics have a certain minimum pulse pair resolution time, which, for the 100-MHz units from DSP Technology that were used in the SRL during the CAMEX-3 campaign, was approximately 10 ns. The maximum measurable corresponding count rate is 100 MHz. However, this maximum count rate will be obtained only for a perfectly periodic input pulse train. The Raman lidar photon counting signals obey Poisson statistics and thus, for a certain mean count rate during a 1-min data acquisition time, the effective count rate for each laser pulse can vary significantly. For example, with a 1-μs bin width in the photon counters, a 40-MHz signal would correspond to 40 counts in a bin. The Poisson probability distribution for n counts with μ mean is given by

$$P(n, \mu) = \frac{e^{-\mu}\mu^{n}}{n!}, \tag{B1}$$

where $P(n, \mu)$ is the probability of measuring n counts in a time interval where the mean number of counts per time interval is μ. Figure 12 shows this distribution with a mean of 40. From this figure it is clear that the effective count rate of the signal from each laser pulse can deviate significantly from the 40-MHz average. Thus, from pulse to pulse, there is a varying probability that two pulses may arrive sufficiently closely spaced in time to be seen by the electronics as a single event.

Traditionally, there are two extremes of behavior that counting systems can exhibit: the systems are referred to as paralyzable and nonparalyzable.[73] A paralyzable counting system is one that is unable to provide a second output pulse unless there is a time interval of at least τ between two successive input pulses. If an additional pulse arrives during response time τ, known as the dead time, the dead time of the apparatus is further extended by τ. In this way, at high count rates the unit will be unable to respond and will be paralyzed. Because the fraction of intervals that are longer than τ is given by $\exp(-\tau N_{\text{real}})$, the equation that relates the measured and true counting rates for a paralyzable counter is[73]

$$N_{\text{measured}} = N_{\text{real}} \exp(-\tau N_{\text{real}}), \tag{B2}$$

where N_{measured} is the observed count rate and N_{real} is the actual count rate.

A nonparalyzable counter is one in which response time τ is independent of the arrival of additional counts. In other words, a nonparalyzable counting system will asymptotically approach a maximum counting rate as the actual count rate increases. The equation that describes the relationship of the measured count rate and the true count rate can be derived as follows: For an observed count rate of N_{measured}, the fraction of time during which the counting unit is unable to respond to counts is τN_{measured}, because each observed count will pro-

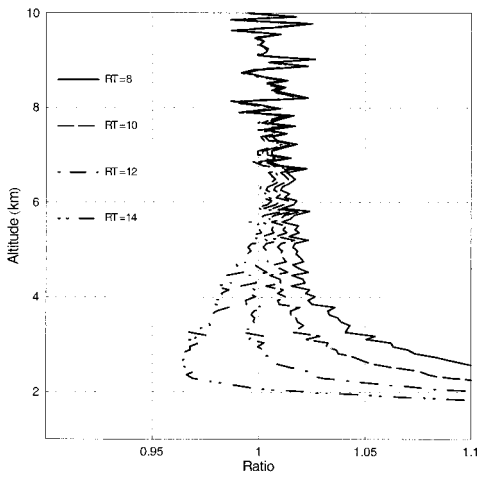

Fig. 14. Comparison of photon pulse pileup corrections for a range of resolving time values for a nonparalyzable count-correction procedure. The resolving time that yields the curve closest to a constant with altitude is chosen for later processing. For the high nitrogen channel shown here, the choice of a resolving time of 11 ns yields a pulse pileup correction that agrees with the low-intensity signal to within ~1% for altitudes above ~3 km.

duce a single dead-time period. Thus the fraction of time during which the unit is sensitive to counts is $1 - \tau N_{\text{measured}}$. The measured count rate may then be expressed as[73]

$$N_{\text{measured}} = (1 - \tau N_{\text{measured}}) N_{\text{real}} \tag{B3}$$

or

$$N_{\text{real}} = \frac{N_{\text{measured}}}{(1 - \tau N_{\text{measured}})}. \tag{B4}$$

These two types of counting system have traditionally been considered extremes of behavior such that the response of a real system would lie somewhere between them. Two curves that represent the paralyzable and the nonparalyzable corrections are plotted in Fig. 13 for $\tau = 10$ ns. For reference, a purely linear response is also shown.

If the count rates are kept low (less than approximately 10–20 MHz in this example), the two equations give similar results. The following example illustrates the use of the nonparalyzable equation. To implement any count saturation correction scheme, one must determine the resolving time of the electronics. In a 100-MHz photon counting system, one would expect that the resolving time parameter would be approximately 10 ns, as stated above. The resolving time's value can be determined empirically from two sets of atmospheric profiles: full-strength profiles and profiles acquired with 10% neutral-density filters in front of all photomultiplier tubes. The nonparalyzable pulse pileup correction is applied to both the full and the reduced-strength signals; then the resolving time value is allowed to be determined for each photomultiplier tube. Figure 14 shows the ratio of the count-corrected, reduced intensity profiles to the count-corrected, full-strength profiles in the high-N_2 channel for resolving times of 8, 10, 12, and 14 ns. Producing the ratios shown in the figure requires the background to be subtracted from each signal. In addition, the reduced intensity and full-strength profiles are normalized to create a value of the ratio of approximately 1.

The resolving time that yields curves that are most nearly constant with altitude was the value chosen for the latter analysis. The value chosen from this figure was 11 ns, in good agreement with the anticipated resolving time for 100-MHz electronics. Figure 15 results from applying the nonparalyzable pulse pileup correction to the high- and low-channel nitrogen data. (During the CAMEX-3 campaign the SRL used two photomultiplier tubes per return wavelength, one for the high-altitude measurement and another for the low. Both of these channels operated in the photon counting mode.) The corrected and uncorrected data are compared in this figure, indicating that only the high-channel data are significantly affected by the correction.

The amount of correction depends on the count rate. The count rates in the high channels are much higher than in the low channels, and thus the correction is greater. In practice, for this 100-MHz system, count rates below 1 MHz are essentially uncorrected and at 10 MHz the correction amounts to ~11%. The count correction affects the high-channel nitrogen data up to an altitude of approximately 4 km. Notice that in the high channels the signal is so intense in the first kilometer that the detectors are saturated and unable to provide useful photon counting data.

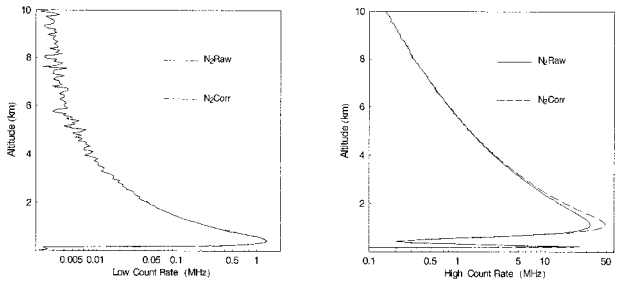

Fig. 15. Low- and high-channel nitrogen data are shown with and without the nonparalyzable count correction for a value of 11 ns for the dead time. The correction is apparent only above approximately 1 MHz, so the correction has much more effect on the high channel data.

1. Modeling of Nonlinear Photon Pile-Up

The two traditional models of pulse pileup described above can produce only a measured count rate that is less than the true count rate. However, real photon counting systems are actually able to display both count loss and count gain. Count gain can result in superlinear photon counting behavior; the measured number of counts can increase faster than the actual number of signal counts. A significant contribution[74] to the understanding of real photon counting systems resulted from a model of the overlapping of

photon pulses that allows for an apparent loss of counts as well as an apparent gain of counts. That mathematical model accounts for the fact that various numbers of photons that might individually not be counted may add together to exceed the threshold and thus be counted. The model developed has the form[74]

$$N = S\,\exp(-\tau_d S)\left[P_{(a)} + P_{(1b\cap 2a)}(\tau_d S) + P_{(2b\cap 3a)}\frac{(\tau_d S)^2}{2} + P_{(3b\cap 4a)}\frac{(\tau_d S)^3}{3!} + \ \ldots\ \right], \quad \text{(B5)}$$

where N is the measured count rate, S is the true count rate, τ_d is the system dead time, $P_{(a)}$ is the probability that a single photon will be above the discriminator threshold, and $P_{(nb\cap[n+1]a)}$ is the probability that n pulses arriving close together will be below the threshold but that $n + 1$ pulses arriving together will be above the threshold. One of the difficulties in implementing Eq. (B5) is the fact that it is double valued. Inasmuch as the equation describes a counting system that is subject to paralysis, there will be two values of real count rate that can yield the observed measured count rate. In the analysis to follow, the correction was limited to the lower-count-rate regime to avoid this complication.

The correction with Eq. (B5) requires both the true count rate, S, and the measured count rate, N. These were determined by acquisition of atmospheric nitrogen data both at full intensity and with an ~1% transmission neutral-density filter installed. The data acquired with the neutral-density filter in place were considered to be proportional to the true count rate because the count rate was reduced sufficiently to minimize the probability of pulse pileup. An accurate transmission value of the filter was determined by normalizing the full and 1% data at a point where the count rates were low for both of these data sets. The 1% data were then divided by the filter transmission determined by this procedure to give the true count-rate curve, S, in Eq. (B5). An array of ordered pairs could then be formed of $\{N_{\text{real}}, N_{\text{meas}}\}$. This array of pairs is the data set that must be fitted by nonlinear Eq. (B5). The general nonlinear regression routine in the Mathematica computer program was used to fit this equation to the data. Using two terms within the brackets of Eq. (B5) yielded the best-fit values $\tau_d = 10.2$ ns, $P_{(a)} = 0.616$, and $P_{(1b\cap 2a)} = 0.266$. Using three terms for the equation yielded $\tau_d = 10.8$ ns, $P_{(a)} = 0.579$, $P_{(1b\cap 2a)} = 0.278$, and $P_{(2b\cap 3a)} = 0.074$. The resolving time determined from this precedure agrees well with the simpler procedure shown in Fig. 14.

A strict physical interpretation of these values in terms of the model would indicate that when the two- (three-) term expression for Eq. (B5) is used the resolving time is 10.2 (10.8) ns, the probability that a count is registered by a single photon exceeding the threshold is approximately 61% (58%), and the probability that a count is registered by two closely spaced photons that would otherwise not be counted is approximately 27% (28%). For the three-term equation the probability that a count is registered because three photons add together is ~7%. The coefficients do not add to 1, which can perhaps be taken as an indication either of the uncertainty in the results or that the physics of the model used to create the equation are not exactly the physics of the counter electronics. The real value of this technique is determined by whether it extends the useful count range of the instruments and not by whether the strict physical interpretation of the results is sensible.

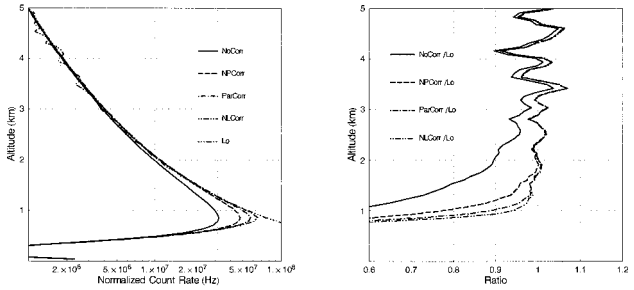

Fig. 16. Comparison of several methods of correcting for the effects of photon pulse pileup. The same nitrogen data treated in Fig. 15 are again analyzed here. The raw data (NoCorr) are shown along with nonparalyzable, paralyzable, and nonlinear corrections (NPCorr, ParCorr, and NLCorr, respectively). The low-channel data (Lo), normalized to the high count rate (in hertz), are also shown as an indication of the true count rate.

At this point the goodness of fit of the two- and three-term forms of Eq. (B5) were compared to see how well they reproduced the true data set. The two equations were nearly indistinguishable in this respect. For simplicity, then, the two-term results were used. To assess the performance of the nonlinear correction scheme, the same set of high-channel data shown in Fig. 15 were analyzed with no correction, with the nonparalyzable correction described above, with a paralyzable correction, and with the nonlinear correction. The results are plotted in Fig. 16. The paralyzable correction is double valued in the same way as the nonlinear results discussed above. As with the nonlinear results, only the low-count-rate solution is displayed here.

In Fig. 16 the low-channel data can be taken as indicative of the shape of the linear, unsaturated profile because the actual count rate for the low channel did not exceed 1 MHz and pulse pileup effects are much less than 1% at this count rate. For comparison purposes, therefore, the low-channel data have been normalized to the high-channel profiles. In increasing order of correction, or closeness to the low-channel data, the processed nitrogen profiles are raw data, nonparalyzable corrected, paralyzable corrected, and nonlinear corrected. The first two of these curves are the same as shown in Fig. 15 but are displayed at the left in terms of count rate in hertz and at the right as a ratio of the corrected results to the normalized low-channel results. The figure re-

veals that the raw data diverge significantly from the low-channel results below an altitude of approximately 4 km. The corresponding altitudes (count rates) for the nonparalyzable, the paralyzable, and the nonlinear corrected results are approximately 2.2 km (7 MHz), 1.4 km (20 MHz), and 1.2 km (40 MHz). Therefore the nonlinear correction would allow the high-channel data to be used to a lower altitude than either the nonparalyzable or the paralyzable corrected data, although the improvement compared with the paralyzable results is relatively small.

2. Photon Pileup Correction in Data Processing

Although the nonlinear and paralyzable procedures permit photon counting data to be used at higher count rates than does the nonparalyzable correction technique, the results of correcting the high-channel data by use of the simpler nonparalyzable approach were sufficient to permit merging of the high-channel data with the low-channel data at an altitude where the low channel is still providing a good signal, as shown in Fig. 15. In addition, the nonlinear technique can fail to converge, and, for both the nonlinear and the paralyzable correction techniques, the low and high solutions may not be consistent. This result is taken to be due to the inherent difficulty of applying the large correction to photon counting data that is implied through the use of the high solution in either the nonlinear or the paralyzable approach. Because of these considerations, the general photon counting SRL measurements during the CAMEX-3 campaign were made such that (1) the low-channel count rate was low enough at every altitude to require essentially no pulse pileup correction and (2) there was a region of overlap between the low and high channels where they were both out of count saturation and could be merged reliably. In this way, the simple procedure of the nonparalyzable count correction could be used satisfactorily. The results presented in this paper were therefore obtained by use of the nonparalyzable correction technique.

Support for this activity has come from the NASA Dynamics and Remote Sensing and Radiation Sciences programs as well as the U.S. Department of Energy's Atmospheric Radiation Measurements program. The author is grateful to J. M. Fernandez for helpful conversations concerning the modeling of the Raman water-vapor spectrum.

References

1. S. H. Melfi, D. N. Whiteman, and R. A. Ferrare, "Observation of atmospheric fronts using Raman lidar moisture measurements," J. Appl. Meteorol. **28,** 789–806 (1989).
2. R. A. Ferrare, S. H. Melfi, D. N. Whiteman, and K. D. Evans, "Raman lidar measurements of Pinatubo aerosols over southeastern Kansas during November–December 1991," Geophys. Res. Lett. **19,** 1599–1602 (1992).
3. A. J. Behrendt and J. Reichardt, "Atmospheric temperature profiling in the presence of clouds with a pure rotational Raman lidar by use of an interference-filter-based polychromator," Appl. Opt. **39,** 1372–1378 (2000).
4. D. D. Turner and J. E. M. Goldsmith, "Twenty-four-hour Raman lidar water vapor measurements during the atmospheric radiation measurement program's 1996 and 1997 water vapor intensive observation periods," J. Atmos. Ocean. Tech. **16,** 1062–1076 (1999).
5. D. N. Whiteman and S. H. Melfi, "Cloud liquid water, mean droplet radius and number density measurements using a Raman lidar," J. Geophys. Res. **104,** 31411–31419 (1999).
6. A. Ansmann, U. Wandinger, M. Riebesell, C. Weitkamp, and W. Michaelis, "Independent measurement of extinction and backscatter profiles in cirrus clouds by using a combined Raman elastic-backscatter lidar," Appl. Opt. **31,** 7113–7131 (1992).
7. J. Reichardt, S. Reichardt, M. Hess, and T. J. McGee, "Correlations among the optical properties of cirrus-cloud particles: microphysical interpretation," J. Geophys. Res. **107,** 4562–4573 (2002).
8. D. N. Whiteman, K. D. Evans, B. Demoz, D. O'C. Starr, D. Tobin, W. Feltz, G. J. Jedlovec, S. I. Gutman, G. K. Schwemmer, M. Cadirola, S. H. Melfi, and F. J. Schmidlin, "Raman lidar measurements of water vapor and cirrus clouds during the passage of hurricane Bonnie," J. Geophys. Res. **106,** 5211–5225 (2001).
9. R. A. Ferrare, S. H. Melfi, D. N. Whiteman, K. D. Evans, and R. Leifer, "Raman lidar measurements of aerosol extinction and backscattering. 1. Methods and comparisons," J. Geophys. Res. **103,** 19663–19672 (1998).
10. B. B. Demoz, D.O'C. Starr, D. N. Whiteman, K. D. Evans, and D. Hlavka, "Raman lidar detection of cloud base," Geophys. Res. Lett. **27,** 1899–1902 (2000).
11. D. Müller, K. Franke, F. Wagner, D. Althausen, A. Ansmann, and J. Heintzenberg, "Vertical profiling of optical and physical particle properties over the tropical Indian Ocean with six-wavelength lidar. 1. Seasonal cycle," J. Geophys. Res. **106,** 28567–28575 (2001).
12. D. Müller, K. Franke, F. Wagner, D. Althausen, A. Ansmann, J. Heintzenberg, and G. Verver, "Vertical profiling of optical and physical particle properties over the tropical Indian Ocean with six-wavelength lidar. 2. Case studies," J. Geophys. Res. **106,** 28577–28595 (2001).
13. D. N. Whiteman, G. Schwemmer, T. Berkoff, H. Plotkin, L. Ramos-Izquierdo, and G. Pappalardo, "Performance modeling of an airborne Raman water vapor lidar," Appl. Opt. **40,** 375–390 (2001).
14. S. H. Melfi, "Remote measurement of the atmosphere using Raman scattering," Appl. Opt. **11,** 1605–1610 (1972).
15. S. H. Melfi and D. Whiteman, "Observation of lower-atmospheric moisture structure and its evolution using a Raman lidar," Bull. Am. Meteorol. Soc. **66,** 1288–1292 (1985).
16. G. Vaughan, D. P. Wareing, L. Thomas, and V. Mitev, "Humidity measurements in the free troposphere using Raman backscatter," Q. J. R. Meteorol. Soc. **114,** 1471–1484 (1988).
17. D. N. Whiteman, S. H. Melfi, and R. A. Ferrare, "Raman lidar system for the measurement of water vapor and aerosols in the Earth's atmosphere," Appl. Opt. **31,** 3068–3082 (1992).
18. A. Ansmann, M. Riebesell, C. Weitkamp, E. Voss, W. Lahmann, and W. Michaelis, "Combined Raman elastic-backscatter lidar for vertical profiling of moisture, aerosol extinction, backscatter, and lidar ratio," Appl. Phys. B **55,** 18–28 (1992).
19. J. E. M. Goldsmith, F. H. Blair, S. E. Bisson, and D. D. Turner, "Turn-key Raman lidar for profiling atmospheric water vapor, clouds, and aerosols," Appl. Opt. **37,** 4979–4990 (1998).
20. D. D. Turner, R. A. Ferrare, L. A. H. Brasseur, and W. F. Feltz, "Automated retrievals of water vapor and aerosol profiles from an operational Raman lidar," J. Atmos. Ocean. Tech. **19,** 37–50 (2002).
21. J. Bösenberg, A. Ansmann, J. Baldasano, D. Balis, C. Böck-

mann, B. Calpini, A. Chaikovsky, P. Flamant, A. Hågård, V. Mitev, A. Papayannis, J. Pelon, D. Resendes, J. Schneider, N. Spinelli, T. Trickl, G. Vaughan, G. Visconti, and M. Wiegner, "EARLINET: European Aerosol Research Lidar Network," presented at the 20th International Laser Radar Conference, Vichy, France, 10–14 July 2000.
22. J. Schneider, D. Balis, C. Böckmann, J. Bösenberg, B. Calpini, A. Chaikovsky, A. Comeron, P. Flamant, V. Freudenthaler, A. Håagård, I. Mattis, V. Mitev, A. Papayannis, G. Pappalardo, J. Pelon, M. Perrone, D. Resendes, N. Spinelli, T. Trickl, G. Vaughan, and G. Visconti, "A European aerosol research lidar network to establish an aerosol climatology (EARLINET)," J. Aerosol Sci. **31,** Suppl. 1, 592–593 (2000).
23. C. M. Penney, R. L. St. Peters, and M. Lapp, "Absolute rotational Raman cross sections for N_2, O_2, and CO_2," J. Opt. Soc. Am. **64,** 712–716 (1976).
24. G. Vaughan, D. P. Wareing, S. J. Pepler, L. Thomas, and V. Mitev, "Atmospheric temperature measurements made by rotational Raman scattering," Appl. Opt. **32,** 2758–2764 (1993).
25. Y. Arshinov and S. Bobrovnikov, "Use of a Fabry–Perot interferometer to isolate pure rotational Raman spectra of diatomic molecules," Appl. Opt. **38,** 4635–4638 (1999).
26. J. A. Salzman and T. A. Coney, "Remote measurement of atmospheric temperatures by Raman lidar," NASA Tech. Memo. TM X-68250 (NASA, Washington, D.C., 1973).
27. G. Herzberg, *Spectra of Diatomic Molecules*, Vol. 1 of Molecular Spectra and Molecular Structure (Kreiger, Malabar, Fla., 1989).
28. D. N. Whiteman, "Examination of the traditional Raman lidar technique. II. Evaluating the ratios for water vapor and aerosols," Appl. Opt. **42,** 2593–2608 (2003).
29. A. T. Young, "Revised depolarization corrections for atmospheric extinction," Appl. Opt. **19,** 3427–3428 (1980).
30. A. T. Young, "On the Rayleigh-scattering optical depth of the atmosphere," J. Appl. Meteorol. **20,** 328–330 (1980).
31. Lord Rayleigh, "On the light from the sky, its polarization and color," Philos. Mag. **41,** 107–120, 274–279 (1871).
32. Lord Rayleigh, "On the scattering of light by small particles," Philos. Mag. **41,** 447–454 (1871).
33. M. Born and E. Wolf, *Principles of Optics* (Cambridge U. Press, Cambridge, 1999).
34. R. M. Measures, *Laser Remote Sensing Fundamentals and Applications* (Wiley-Interscience, New York, 1984).
35. V. Sherlock, A. Hauchecorne, and J. Lenoble, "Methodology for the independent calibration of Raman backscatter water-vapor lidar systems," Appl. Opt. **38,** 5816–5837 (1999).
36. G. Avila, J. M. Fernandez, B. Mate, G. Tejeda, and S. Montero, "Ro-vibrational Raman cross sections of water vapor in the OH stretching region," J. Mol. Spectrosc. **196,** 77–92 (1999).
37. D. N. Whiteman, W. F. Murphy, N. W. Walsh, and K. D. Evans, "Temperature sensitivity of an atmospheric Raman lidar system based on a XeF excimer laser," Opt. Lett. **18,** 247–249 (1993).
38. D. N. Whiteman, G. E. Walrafen, W.-H. Yang, and S. H. Melfi, "Measurement of an isosbestic point in the Raman spectrum of liquid water using a backscattering geometry," Appl. Opt. **38,** 2614–2615 (1999).
39. M. Mitev, I. V. Grigorov, and V. B. Simeonov, "Lidar measurement of atmospheric aerosol extinction profiles: a comparison between 2 techniques—Klett inversion and pure rotational Raman-scattering methods," Appl. Opt. **31,** 6469–6474 (1992).
40. W. S. Heaps, J. Burris, and J. A. French, "Lidar technique for remote measurement of temperature by use of vibrational–rotational Raman spectroscopy," Appl. Opt. **36,** 9402–9405 (1997).
41. W. F. Murphy, "Ro-vibrational Raman-spectrum of water-vapor nu-2 and 2-nu-(2)," Mol. Phys. **33,** 1701–1714 (1977).
42. W. F. Murphy, "Ro-vibrational Raman-spectrum of water-vapor nu-1 and nu-3," Mol. Phys. **36,** 727–732 (1978).
43. J. M. Fernendez-Sanchez and W. F. Murphy, "Raman-scattering cross sections and polarizability derivatives for H_2S, D_2S and HDS," J. Mol. Spectrosc. **156,** 431–443 (1992).
44. J. M. Fernendez-Sanchez and W. F. Murphy, "True and effective polarizability tensors for asymmetric-top molecules—the rotational Raman-spectra of H2S and D2S," J. Mol. Spectrosc. **156,** 444–460 (1992).
45. J. M. Fernandez, Instituta Estructura Matera, Consejo Superior de Investigaciones Científicas, Serrano 117, 28006, Madrid, Spain (personal communication, 1999).
46. D. A. Long, *Raman Spectroscopy* (McGraw-Hill, New York, 1977).
47. C-Y. She, "Spectral structure of laser light scattering revisited: bandwidths of nonresonant scattering lidars," Appl. Opt. **40,** 4875–4884 (2001).
48. P. A. T. Haris, "Pure rotational Raman lidar for temperature measurements in the lower troposphere," Ph.D. dissertation (Pennsylvania State University, State College, Pa., 1995).
49. M. Bass, ed., *Handbook of Optics* (McGraw-Hill, New York, 1995).
50. National Oceanic and Atmospheric Administration, *U.S. Standard Atmosphere*, NOAA Doc. S/T 76-1562 (National Oceanic and Atmospheric Administration, Washington, D.C., 1976).
51. A. M. Bass and R. J. Paur, "Ultraviolet cross-sections of ozone. I. Measurements," in *Atmospheric Ozone, Proceedings of the Quadrennial Ozone Symposium*, C. S. Zerophos and A. Ghanzi, eds. (Reidel, Hingham, Mass., 1985).
52. Modtran 4 Radiative Transfer Code (U.S. Air Force Research Laboratory, Hanscom Air Force Base, Mass., 1999).
53. D. R. Bates, "Rayleigh scattering by air," Planet. Space Sci. **32,** 785–790 (1984).
54. A. Bucholtz, "Rayleigh-scattering calculations for the terrestrial atmosphere," Appl. Opt. **34,** 2765–2773 (1995).
55. E. R. Peck and K. Reeder, "Dispersion of air," J. Opt. Soc. Am. **62,** 958–962 (1972).
56. R. M. Goody and Y. L. Yung, *Atmospheric Radiation Theoretical Basis* (Oxford U. Press, Oxford, 1989).
57. S. Chandrasekhar, *Radiative Transfer* (Dover, New York, 1960).
58. A. Ansmann, M. Riebesell, and C. Weitkamp, "Measurement of atmospheric aerosol extinction profiles with a Raman lidar," Opt. Lett. **15,** 746–748 (1990).
59. R. T. H. Collis and P. B. Russell, "Lidar measurement of particles and gases by elastic backscattering and differential absorption," in *Laser Monitoring of the Atmosphere*, E. D. Hinkley, ed. (Springer-Verlag, Berlin, 1976).
60. D. N. Whiteman, "Application of statistical methods to the determination of slope in lidar data," Appl. Opt. **38,** 3360–3369 (1999).
61. E. P. Shettle and R. W. Fenn, "Models for the aerosols of the lower atmosphere and the effects of humidity variations on their optical properties," Doc. AFGL-TR-79-0214 (U.S. Air Force Geophysics Laboratory, Hanscom Air Force Base, Mass., 1979).
62. E. P. Hamonou, P. Chazette, D. Balis, F. Dulac, X. Schneider, E. Galani, G. Ancellet, and A. Papayannis, "Characterization of the vertical structure of Saharan dust export to the Mediterranean basin," J. Geophys. Res. **104,** 22257–22270 (1999).
63. S. Kato, M. H. Bergin, T. P. Ackerman, T. P. Charlock, E. E. Clothiaux, R. A. Ferrare, R. N. Halthore, N. Laulainen, G. G. Mace, J. Michalsky, and D. D. Turner, "A comparison of the aerosol thickness derived from ground-based and airborne measurements," J. Geophys. Res. **105,** 14701–14717 (2000).
64. T. Eck, Aeronet Group, NASA/Goddard Space Flight Center, Greenbelt, Md. 20771 (personal communication, 2002).
65. P. R. Bevington and D. K. Robinson, *Data Reduction and Error*

Analysis for the Physical Sciences (McGraw-Hill, New York, 1992).
66. U. Wandinger, "Multiple-scattering influence on extinction- and backscatter-coefficient measurements with Raman and high-spectral-resolution lidars," Appl. Opt. **37,** 417–427 (1998).
67. E. W. Eloranta, "Practical model for the calculation of multiply scattered lidar returns," Appl. Opt. **37,** 2464–2472 (1998).
68. T. N. Carlson and J. M. Prospero, "The large-scale movement of Saharan air outbreakes over the northern equatorial Atlantic," J. Appl. Meteorol. **11,** 283–297 (1972).
69. J. M. Prospero, R. A. Glaccum, and R. T. Nees, "Atmospheric transport of soil dust from Africa to South America," Nature **289,** 570–572 (1981).
70. L. Schutz, R. Jaenicke, and H. Pietrek, "Saharan dust transport over the North Atlantic Ocean," Geol. Special Paper 186 (Geological Society of America, Boulder, Colo., 1981), pp. 87–100.
71. A. di Sarra, T. Di Iorio, M. Cacciani, G. Fiocco, and D. Fuà, "Saharan dust profiles measured by lidar at Lampedusa," J. Geophys. Res. **106,** 10335–10347 (2001).
72. O. Dubovik, B. Holben, T. Eck, A. Smirnnov, Y. Kaufman, M. King, D. Tanre, and I. Slutsker, "Variability of absorption and optical properties of key aerosol types observed in worldwide locations," J. Atmos. Sci. **59,** 590–608 (2002).
73. R. D. Evans, *The Atomic Nucleus* (McGraw-Hill, New York, 1955).
74. D. P. Donovan, J. A. Whiteway, and A. I. Carswell, "Correction for nonlinear photon-counting effects in lidar systems," Appl. Opt. **32,** 6742–6753 (1993).